Citation: Xu, X. and Lagor, F. D. "Quasi-steady effective angle of attack and its use in lift-equivalent motion design." AIAA Journal, 2021. DOI: https://doi.org/10.2514/1.J059663

Quasi-Steady Effective Angle of Attack and Its Use in Lift-Equivalent Motion Design*

Xianzhang Xu† and Francis D. Lagor‡
University at Buffalo, The State University of New York, Buffalo NY 14260

The effective angle of attack of an airfoil is a composite mathematical expression from quasi-steady thin-airfoil theory that combines the geometric contribution to angle of attack with pitching and plunging effects. For a maneuvering airfoil, the instantaneous effective angle of attack is a virtual angle that corresponds to the equivalent lift based on a steady, lift versus angle of attack curve. The existing expression for effective angle of attack depends on attached-flow, thin-airfoil, small-angle, and small-camber-slope assumptions. This paper derives a new expression for effective angle of attack that relaxes the small-angle and small-camber-slope assumptions. The new expression includes effects from pitching, plunging, and surging motions, as well as spatial nonuniformity of the flow. The proposed expression simplifies to the existing quasi-steady expression by invoking the appropriate assumptions. Further, the proposed expression leads to a replacement for the classic, zero-lift angle of attack equation for steady flow past a thin airfoil, which is compared to experimental values for cambered NACA 4-digit airfoils. The new expression is also used for lift-equivalent motion design for a maneuvering airfoil to emulate the effective angle of attack of a non-maneuvering airfoil encountering a transverse gust under a quasi-steady assumption. Computational Fluid Dynamics simulations support the use of the proposed effective angle of attack expression for lift-equivalent motion design, subject to an attached-flow assumption.

I. Nomenclature

Greek Letters

$\alpha, \dot{\alpha}$	=	angle of attack, angle of attack rate
α_{eff}	=	effective angle of attack
β	=	side-slip angle
γ	=	vortex sheet strength per unit length
Γ	=	total circulation
θ	=	angular coordinate along mean camber line
$\tilde{\theta}$	=	dummy angle for angular identities
θ_0	=	angular coordinate of evaluation location on mean camber line
$\theta_g, \dot{\theta}_g$	=	geometric angle of attack, pitch rate
ξ	=	location along camber line
ρ	=	density of air

Roman Letters

a	=	coordinate of pitch axis in semi-chords
A_n, B_n	=	Fourier series coefficients in thin-airfoil theory
C_n, D_n	=	Fourier series coefficients for pitching and plunging control signals
b	=	semi-chord length, $c/2$
c	=	chord length
C	=	name of center of rotation point
C_l	=	sectional lift coefficient
dz/dx	=	slope of the mean camber line
G	=	name of center of mass point

*A preliminary version was presented as Paper 2020-1782 at the AIAA SciTech 2020 Forum, Orlando, FL, January 6-10,2020.

†Graduate Student, Department of Mechanical and Aerospace Engineering, AIAA Student Member
‡Assistant Professor, Department of Mechanical and Aerospace Engineering, AIAA Senior Member, email: flagor@buffalo.edu

$\dot{h}$	=	plunge rate
k	=	reduced frequency
L	=	gust width
L'	=	lift per unit length
N	=	name of leading edge point (nose) of airfoil
O	=	name of origin point for inertial frame
P	=	name of point along the camber line
Re_c	=	chord-based Reynolds number
$\dot{s}$	=	surge rate
$\overline{V}$	=	constant, characteristic flow speed
$\overline{V}_\mathrm{n}$	=	nondimensionalized flow component normal to the camber line
V_∞	=	magnitude of freestream velocity
$V_{\infty,\mathrm{n}}$	=	magnitude of normal component of freestream velocity
V_g	=	maximum velocity of gust encounter
w_in	=	induced flow component
$w_{\mathrm{in,n}}$	=	component of induced velocity normal to the camber line

Vectors, Reference Frames, Components

$\mathcal{B}$	=	Body-fixed reference frame
$\hat{\boldsymbol{b}}_x, \hat{\boldsymbol{b}}_y, \hat{\boldsymbol{b}}_z$	=	basis vectors of the body frame
$\hat{\boldsymbol{e}}_x, \hat{\boldsymbol{e}}_z$	=	basis vectors of frame $\mathcal{I}$
$\mathcal{I}$	=	Inertial reference frame fixed in space at point O
$\hat{\boldsymbol{n}}_x, \hat{\boldsymbol{n}}_z$	=	basis vectors of frame $\mathcal{N}$
$\mathcal{N}$	=	Body-fixed reference frame at point N, the nose of the airfoil
$\boldsymbol{r}_{P/O}$	=	position vector of point P relative to point O
$\mathcal{R}$	=	Rotating reference frame located at point C, the axis of rotation
(s, h)	=	coordinates of point C in reference frame $\mathcal{I}$
(u, v, w)	=	components of ${}^{\mathcal{I}}\boldsymbol{v}_{\mathrm{G/O}}$ expressed in the body frame
(u', v', w')	=	components of ${}^{\mathcal{I}}\boldsymbol{v}_{\mathrm{G/flow}}$ expressed in frame $\mathcal{B}$,
	=	components of ${}^{\mathcal{I}}\boldsymbol{v}_{\mathrm{P/flow}}$ expressed in frame $\mathcal{R}$,
	=	components of ${}^{\mathcal{I}}\boldsymbol{v}_{\mathrm{flow/P}}$ expressed in frame $\mathcal{N}$
(u_x, u_z)	=	external flow components in the inertial reference
${}^{\mathcal{I}}\boldsymbol{v}_{\mathrm{G/flow}}$, ${}^{\mathcal{I}}\boldsymbol{v}_{\mathrm{P/flow}}$	=	flow-relative velocity vectors
${}^{\mathcal{I}}\boldsymbol{v}_{G/O}$	=	inertial velocity of point G relative to point O
$\hat{\boldsymbol{w}}_x, \hat{\boldsymbol{w}}_y, \hat{\boldsymbol{w}}_z$	=	basis vectors of the wind frame
${}^{\mathcal{I}}\boldsymbol{\omega}^{\mathcal{R}}$	=	angular velocity of frame $\mathcal{R}$ relative to frame $\mathcal{I}$
$\mathcal{W}$	=	wind frame located at point G
(x, z)	=	coordinates of point P in reference frame $\mathcal{N}$
(x_C, z_C)	=	coordinates of point C in reference frame $\mathcal{N}$

II. Introduction

Thin-airfoil theory has proven to be effective for predicting the aerodynamic forces exerted on airfoils with attached flow and small angles of attack. Steady thin-airfoil theory assumes that a sufficiently thin airfoil with a steady and attached flow can be represented by a thin sheet of vortices along its mean camber line, which acts as a streamline of the flow [1]. Quasi-steady thin airfoil theory, an adaptation of the steady theory, incorporates slowly varying pitch, surge, and plunge motions of the airfoil [2]. As an extension of quasi-steady thin-airfoil theory, the works of Theodorsen [3], Wagner [4], Sears [5], von Kármán [2], and others contributed to the unsteady thin-airfoil theory that examines airfoil motions with prominent acceleration terms and flow or wake unsteadiness. Theodorsen developed an unsteady lift model that includes the effects of added mass and wake vorticity [3]. Wagner proposed an unsteady aerodynamic model similar to Theodorsen's that simulates the response of a step change in angle of attack [4]. Although many of these models have limiting assumptions for inviscid, incompressible, and attached flow, they are still widely used as fundamental tools in unsteady aerodynamics research [6].

The motion of a wing in a flowfield is considered quasi-steady provided that the aerodynamic forces can be written as static outputs of the flow parameters [7]. A quasi-steady assumption may be made when unsteady effects are very small and may be neglected [8]. Unsteadiness can be categorized using the reduced frequency

$$k = \frac{\omega b}{V_\infty}, \tag{1}$$

where ω is a characteristic angular frequency, b is the semi-chord, and V_∞ is the freestream flow speed. If $k = 0$, the airfoil is not maneuvering, and the flow condition is steady [8]. A common definition for the quasi-steady regime is $0 \leq k \leq 0.05$ [8]. However, Brunton et al. [7] have shown that at low Reynolds numbers, a quasi-steady assumption holds well for a sinusoidally plunging plate up to $k = 0.25$. Motions with larger reduced frequencies are generally considered to require unsteady modeling.

Across the steady, quasi-steady, and unsteady thin-airfoil theories, a useful concept for comparing the lift generated by various airfoil motions is effective angle of attack. The effective angle of attack of an airfoil represents a composite view of the flow along the airfoil that considers various sources of flow-relative motion. Leishman [8] presented an effective angle of attack for a quasi-steady thin airfoil undergoing pitching and plunging maneuvers using the concept of virtual camber. Sedky et al. [9] included transverse gust effects into this expression with the use of virtual camber. Peters [10, 11] and Peters et al. [12] combined unsteady motions through large angles and unsteady freestream effects into a comprehensive, state-space airloads model. Continuing the state-space modeling approach, Brunton et al. [13] investigated the lift generation of a pure plunging flat plate through 2D simulation, and the effective angle of attack was applied as a state variable in their empirical state-space representations of Theodorsen's lift model. Ramesh et al. [14] used the Leading Edge Suction Parameter (LESP), which is related the effective angle of attack through the zeroth Fourier coefficient of the airfoil's bound circulation, to modulate the shedding of vorticity at the leading edge in a discrete-vortex model. Several authors have also used either the effective angle of attack or the LESP as an internal state variable in a dynamic model of the lift. For example, Sedky et al. [9] incorporated the effective angle of attack as a state variable in a dynamic Goman-Khrabrov (GK) model for a pitching wing. Narsipur et al. [15] similarly incorporated the related LESP quantity as a state variable in a GK model.

Visbal and Garmann [16] used the effective angle of attack as a tool for interpreting the state of the wing when analyzing lift-equivalent motions for pitching and plunging. Many other works [9, 13, 16–18] have also used effective angle of attack due to its ability to incorporate kinematic effects and its interpretability, even though applications with separated flow, large amplitude motions, or large amplitude gust encounters often violate the assumptions underlying the effective angle of attack derivation from thin-airfoil theory. Given the common use of effective angle of attack, this paper seeks to reduce the number of assumptions involved in its derivation by removing the small-angle and small-camber-slope assumptions. Some works [9, 13, 16] consider effective angle of attack as an integral, composite quantity for the wing, while other works [17, 18] apply the effective angle of attack at a single point on the chord. This paper seeks to unify the terminology by presenting a composite (i.e., spatially integrated) effective angle of attack expression that accounts for variety of flow conditions and kinematics.

A new expression is derived based on three modifications to the derivation of effective angle of attack presented in [8]: (i) we include a formal kinematic analysis for the motion of an arbitrary point on the mean camber line of the airfoil to include all quasi-steady kinematic contributions (e.g., pitching, plunging, and surging motions); (ii) we utilize an expression of angle of attack based on the relative velocity of the fluid to include freestream nonuniformity (e.g., gusts) and apply it locally at each point on the camber line; and (iii) we incorporate useful trigonometric identities to retain nonlinearities that would otherwise be removed by simplifying assumptions. These alterations produce a useful effective angle of attack expression that includes the effects of surging, plunging, and pitching motion, as well as free stream nonuniformity.

Freestream nonuniformity refers to spatial variation in the freestream velocity distribution. Understanding the aerodynamic forces occurring in the presence of freestream nonuniformity is relevant to flow disturbance problems for aircraft, including gust encounters [19] and landing in the presence of wind shear [20]. Progress has been made on specific classes of nonuniformity. For example, recent works by Hammer et al. [21] and Naguib and Koochesfahani [20] have investigated the effects of shear flow on a 2D symmetric airfoil and a moving cylinder, respectively. The present work applies to thin airfoils and requires that the velocity distribution be known. Due to use of the Kutta-Joukowski theorem [1], which establishes the proportional relationship between sectional lift and bound circulation in an airfoil, the velocity distribution in the proposed effective angle of attack must also correspond to a potential (i.e., irrotational) flow. If the flow is not a potential flow, the effective angle of attack expression can still be evaluated using a known velocity distribution, however, the resulting value must be regarded as an approximate solution under the assumption of the Kutta-Joukowski relation between lift and the circulation. Although, this quantity is not rigorous, it may be useful. Sections VII and VIII calculate the (approximate) effective angle of attack for an airfoil encountering a transverse gust described by a sine-squared vertical velocity profile. The CFD results of Section VIII show that the effective angle of attack can provide a reasonable prediction of the lift force during a transverse gust encounter, subject to the attached flow assumption used in its derivation.

The new expression has a reduced dependence on the small-angle and small-camber-slope assumptions. Although we do not explicitly invoke a small-angle assumption, the assumption of flow attachment implicitly limits the work to relatively small angles. Similarly, we remove the small-camber-slope assumption from the derivation, however, it still partially appears (implicitly) in a derivation step that projects the bound circulation onto the horizontal axis. Nonetheless, our new expression is a useful extension of the previous expression for effective angle of attack from quasi-steady thin airfoil theory. Additionally, in contrast to other methods of calculating an effective angle of attack (e.g., see [8]), our approach does not require calculation of a virtual camber, thereby simplifying the calculation and allowing effective angle of attack to be applied to (physically) cambered airfoils.

Several special cases can be derived from the proposed expression. For a pitching and plunging airfoil without camber, re-applying the small-angle and small-camber-slope assumptions yields the classic expression for quasi-steady effective angle of attack. For examining the angle of attack contribution due to a transverse flow, the proposed expression provides the correct proportional relationship between lift and components of the flow velocity. Comparison is made to experimental data of the zero-lift angle for steady flow past cambered airfoils. The proposed expression provides a minor deviation from the existing theory, yielding zero-lift angles that are smaller in magnitude than the existing theory. In Section VIII, Computational Fluid Dynamics (CFD) simulations are presented for steady flow past a NACA 0012, 2412 and 6412 airfoils, which allows for a comparison between the existing theory, the proposed theory, and CFD results.

A useful application for the proposed effective angle of attack expression is to compare disparate aerodynamic scenarios. Leung et al. [17] designed motions of a wing to replicate a transverse gust encounter by calculating a pointwise effective angle of attack at representation locations on the airfoil chord. Using a composite (i.e., non-local) version of effective angle of attack, we construct a framework for lift-equivalent motion design under a quasi-steady assumption. In particular, we formulate an optimal control problem that designs an optimal maneuver for an airfoil to match a desired effective angle of attack profile. We apply the framework to design a motion profile for a maneuvering airfoil that emulates the aerodynamic response of a non-maneuvering airfoil during a transverse gust encounter. Section VII shows that different solutions to match the effective angle of attack are possible depending on the type of motion inputs, the number of inputs, and the initial guess of the inputs.

The outline of this paper is as follows: Section III reviews effective angle of attack in classical thin-airfoil theory. Section IV provides a kinematic analysis of motion of an arbitrary point on the mean camber line of a thin airfoil. Section V uses the kinematics of the airfoil, an expression for angle of attack from aircraft flight dynamics applied locally, and trigonometric identities to derive a new expression for effective angle of attack. Section VI examines special cases of the expression, and Section VII uses the expression to create a framework for applications that involve creating an airfoil motion profile that matches a desired effective angle of attack trajectory. Section VIII presents CFD simulations to examine the performance of the proposed theory for steady-flow conditions and in the design of a lift-equivalent pitching maneuver to mimic a gust encounter. Section IX concludes the paper and discusses ongoing work.

III. Effective Angle of Attack in Thin-Airfoil Theory

This section reviews thin airfoil theory as detailed by Anderson in [1] and the derivation of a prior expression for effective angle of attack as presented by Leishman in [8].

Thin-airfoil theory provides a potential-flow-based method of predicting the aerodynamic loading on an airfoil from the freestream flow conditions and the geometric and kinematic characteristics of the airfoil. Thin-airfoil theory represents a sufficiently thin airfoil using a vortex sheet placed along the mean camber line, as shown in Fig. 1(a). For a thin airfoil with chord length c and with small camber, the camber line is close to the chord line. A helpful analytical approximation projects the vortex sheet onto the chord line so that the sheet strength (i.e., the circulation strength per unit length) may be expressed as $\gamma = \gamma(x)$. The vortex sheet must satisfy the Kutta condition that the flow leaves smoothly at the trailing edge of the airfoil [1], which results in an end condition of $\gamma(c) = 0$. The vortex sheet acts as a streamline of the flow so that the velocity component normal to the camber line must be zero at all points along the camber line [1]. Determining the proper circulation-strength distribution to meet these requirements results in a total circulation that can be used to determine the lift force and pitching moment experienced by the airfoil [1].

Let $w_{\text{in,n}}$ be the component of the flow velocity induced by the vortex sheet that is normal to the camber line (i.e., the

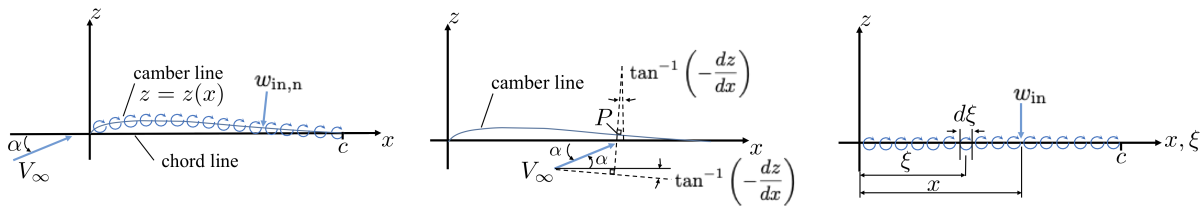

(a) (b) (c)

Fig. 1 a) Vortex sheet on the mean camber line. b) Geometry for finding the normal component of freestream velocity $V_{\infty,\mathrm{n}}$. c) Velocity induced by the vortex sheet on the chord line. (Figures adapted from [1].)

induced flow component arising from vortex sheet elements along the camber line). For camber line to be a streamline, the normal component of the impinging flow and the normal component of the velocity induced by the vortex sheet must cancel such that

$$V_{\infty,\mathrm{n}} + w_{\mathrm{in,n}} = 0, \tag{2}$$

where $V_{\infty,\mathrm{n}}$ is the normal component of the freestream velocity that can be found by inspection of Fig. 1(b). The slope of camber line is dz/dx, and Fig. 1(b) shows that

$$V_{\infty,\mathrm{n}} = V_\infty \sin\left(\alpha + \tan^{-1}\left(-\frac{dz}{dx}\right)\right). \tag{3}$$

Classical thin-airfoil theory makes a small-angle assumption, $\sin\tilde{\theta} \approx \tan\tilde{\theta} \approx \tilde{\theta}$, to simplify (3), such that

$$V_{\infty,\mathrm{n}} = V_\infty \left(\alpha - \frac{dz}{dx}\right). \tag{4}$$

Thin-airfoil theory also simplifies calculations by placing the vortex sheet on the chord line (i.e., assuming the airfoil's camber is small). Figure 1(c) illustrates the calculation of the velocity component w_{in} that is induced by the vortex sheet and is normal to the chord line. The velocity dw_{in} at point x induced by the sheet element at point ξ is given by

$$dw_{\mathrm{in}} = -\frac{\gamma(\xi)d\xi}{2\pi(x-\xi)}. \tag{5}$$

The velocity $w_{\mathrm{in}}(x)$ at point x induced by the vortex sheet can be obtained by integration from the leading edge at $x = 0$ to the trailing edge at $x = c$ such that

$$w_{\mathrm{in}}(x) = -\int_0^c \frac{\gamma(\xi)d\xi}{2\pi(x-\xi)}. \tag{6}$$

Under the assumption that $w_{\mathrm{in}} \approx w_{\mathrm{in,n}}$ and using (2) to equate the normal velocity components to enforce the camber line as a streamline leads to the Fundamental Equation of Thin Airfoil Theory [1]

$$V_\infty \left(\alpha - \frac{dz}{dx}\right) = \frac{1}{2\pi}\int_0^c \frac{\gamma(\xi)d\xi}{x-\xi}. \tag{7}$$

Equation (7) states that normal flow component at point x equals to the induced velocity from the vortex sheet due to the integration of the vortex sheet along the chord. If the flow condition V_∞, geometric flow angle α, and the slope of the camber line dz/dx are specified in (7), the vortex sheet strength $\gamma(\xi)$ can be found to enforce the Kutta condition and satisfy the streamline condition present in (7). However, the left-hand side of the equation is derived based on small-angle and small-camber-slope assumptions. Section V re-visits this derivation and removes these assumptions from this step.

Parameterizing by an angular coordinate θ under the change of variables

$$x = \frac{c}{2}\left(1 - \cos\theta\right), \tag{8}$$

aids in evaluating the integrals involved in solving (7) for $\gamma(\xi)$, leading to

$$V_\infty\left(\alpha - \frac{dz}{dx}\right) = \frac{1}{2\pi}\int_0^\pi \frac{\gamma(\theta)\sin\theta d\theta}{\cos\theta - \cos\theta_0}. \tag{9}$$

The integral equation (9) can be solved for the circulation distribution [1]

$$\gamma(\theta) = 2V_\infty\left(A_0\frac{1+\cos\theta}{\sin\theta} + \sum_{n=1}^{\infty} A_n \sin n\theta\right). \tag{10}$$

Plugging in (10) into (9) and evaluating using the trigonometric integral identities [1]

$$\int_0^\pi \frac{\sin n\theta \sin\theta d\theta}{\cos\theta - \cos\theta_0} = -\pi\cos n\theta_0, \tag{11}$$

and,

$$\int_0^\pi \frac{\cos n\theta d\theta}{\cos\theta - \cos\theta_0} = \frac{\pi\sin n\theta_0}{\sin\theta_0}, \tag{12}$$

leads to the slope of the camber line represented as a cosine series expansion [1]

$$\frac{dz}{dx} = (\alpha - A_0) + \sum_{n=1}^{\infty} A_n \cos n\theta_0. \tag{13}$$

In Fourier analysis, functions of the form $f(\theta) = B_0 + \sum_{n=1}^{\infty} B_n \cos\ n\theta$ have Fourier coefficients that can be found by taking the inner product of both sides with another cosine function and utilizing the orthogonality of cosine harmonics, leading to [1]

$$B_0 = \frac{1}{\pi}\int_0^\pi f(\theta)d\theta \tag{14}$$

$$B_n = \frac{2}{\pi}\int_0^\pi f(\theta)\cos\ n\theta d\theta. \tag{15}$$

Applying this method, the Fourier coefficients of (13) become

$$A_0 = \alpha - \frac{1}{\pi}\int_0^\pi \frac{dz}{dx}d\theta_0, \tag{16}$$

$$A_n = \frac{2}{\pi}\int_0^\pi \frac{dz}{dx}\cos n\theta_0 d\theta_0. \tag{17}$$

The remainder of the derivation of the lift coefficient from thin-airfoil theory follows from integration of the circulation distribution and application of the Kutta-Joukowski theorem. The total circulation of the vortex sheet on the camber line is [1]

$$\Gamma = \int_0^c \gamma(\xi)d\xi = \frac{c}{2}\int_0^\pi \gamma(\theta)\sin\theta d\theta,$$

and plugging in the assumed form of γ gives the total bound circulation

$$\Gamma = \pi c V_\infty\left(A_0 + \frac{A_1}{2}\right). \tag{18}$$

Note that due to integral identity (11) only the A_0 and A_1 Fourier coefficients survive. Using the Kutta-Joukowski theorem, the resulting coefficient of lift per unit span [1]

$$C_l = \frac{L'}{\frac{1}{2}\rho V_\infty^2 c} = \frac{\rho V_\infty \Gamma}{\frac{1}{2}\rho V_\infty^2 c} = 2\pi\left(A_0 + \frac{A_1}{2}\right). \tag{19}$$

The linear relationship $C_l = 2\pi\alpha$ can be compared to (19) and the terms within the parentheses of (19) can be defined as an effective angle of attack

$$\alpha_{\text{eff}} = A_0 + \frac{A_1}{2}. \tag{20}$$

Substitution of (16) and (17) leads to the final expression for the lift coefficient in steady, thin-airfoil theory [1]

$$C_l = 2\pi \underbrace{\left(\alpha + \frac{1}{\pi}\int_0^{\pi} \frac{dz}{dx}\left(\cos\theta_0 - 1\right) d\theta_0\right)}_{\alpha_{\text{eff}}}, \tag{21}$$

in which the integral term incorporates the effect of camber.

For a quasi-steady theory, Leishman [8] gives a textbook derivation of the expression for effective angle of attack for a symmetric, thin airfoil of semi-chord length b that is undergoing pitching and plunging motions. The kinematic motions of the symmetric airfoil induce relative flow velocities along the chord. The resulting lift can be compared to the lift produced by a virtual stationary airfoil with camber and a geometric angle of attack. The kinematic effects due to plunge rate $\dot{h}$ and pitch rate $\dot{\alpha}$ prescribe a distribution of the relative velocity along the chord that can be used to find the virtual camber distribution. Equations (16), (17), and (19) from thin-airfoil theory apply to the virtual airfoil leading to the quasi-steady effective angle of attack [8]

$$\alpha_{\text{eff}} = \alpha + \frac{\dot{h}}{V_\infty} + b\left(\frac{1}{2} - a\right)\frac{\dot{\alpha}}{V_\infty}, \tag{22}$$

where the pitch axis is located a semi-chords from the mid-chord. Sedky et al. [9] use virtual camber to include additional effects from a transverse gust V_g, providing a quasi-steady effective angle of attack

$$\alpha_{\text{eff}} = \alpha + \frac{\dot{h}}{V_\infty} + b\left(\frac{1}{2} - a\right)\frac{\dot{\alpha}}{V_\infty} + \frac{1}{\pi}\int_0^{\pi} \frac{V_g(\theta_0)}{V_\infty}\left(\cos\theta_0 - 1\right) d\theta_0.$$

IV. Local Angle of Attack for a Point on the Camber Line

The motion of an airfoil alters the inertial velocity, i.e., the time rate of change of position vector with respect to the inertial frame, of each point on the camber line. These velocity changes also alter the local velocity relative to the flow and the associated local angle of attack. This section derives the kinematics for an arbitrary point P on the camber line during the two-dimensional motion of an airfoil. Using these kinematics, this section calculates the local angle of attack at point P. The notational conventions in this section are based on [22] for engineering dynamics and [23] for aircraft flight dynamics.

Let $\mathcal{B} = \left(G, \hat{\boldsymbol{b}}_x, \hat{\boldsymbol{b}}_y, \hat{\boldsymbol{b}}_z\right)$ be a body-fixed reference frame (i.e., the body frame) with unit vectors $\hat{\boldsymbol{b}}_x$, $\hat{\boldsymbol{b}}_y$, and $\hat{\boldsymbol{b}}_z$, that is located at the center of mass G of an aircraft flying as shown in Fig. 2(a). In aircraft flight dynamics (e.g., see [23]), it is useful to also construct a reference frame located at the center of mass G that is known as the wind frame $\mathcal{W} = \left(G, \hat{\boldsymbol{w}}_x, \hat{\boldsymbol{w}}_y, \hat{\boldsymbol{w}}_z\right)$. The wind frame has the $\hat{\boldsymbol{w}}_x$ direction aligned in the opposing direction of the relative wind experienced by the aircraft, causing the aerodynamic forces of lift, drag, and side force to act along the reference directions in this frame. To construct the wind frame, rotate the body frame through an angle of attack α about the $-\hat{\boldsymbol{b}}_y$ axis of the body frame, followed by a rotation through a side-slip angle β about the $-\hat{\boldsymbol{b}}_z$ direction. These rotations are left-handed rotations (i.e., rotations about the negative direction of the axis in the right-handed sense) to ensure matching of the definitions of these angles between flight dynamics and historical aerodynamics literature [23]. The wind frame can provide a formal way to calculate the local angle of attack at a point based on kinematics and the flowfield.

Let $\mathcal{I} = (O, \hat{\boldsymbol{e}}_x, \hat{\boldsymbol{e}}_y, \hat{\boldsymbol{e}}_z)$ be an inertial reference frame fixed in space at point O with unit vectors $\hat{\boldsymbol{e}}_x$, $\hat{\boldsymbol{e}}_y$, and $\hat{\boldsymbol{e}}_z$. The aerodynamic characteristics of the aircraft's dynamics are determined by the velocity of the aircraft relative to the surrounding air, which is given by [23]

$${}^{\mathcal{I}}\boldsymbol{v}_{\text{G/flow}} = {}^{\mathcal{I}}\boldsymbol{v}_{G/O} - {}^{\mathcal{I}}\boldsymbol{v}_{\text{flow/O}}, \tag{23}$$

where ${}^{\mathcal{I}}\boldsymbol{v}_{G/O}$ is the inertial velocity of the aircraft's center of mass and ${}^{\mathcal{I}}\boldsymbol{v}_{\text{flow/O}}$ is the inertial velocity of the wind. The left superscript $\mathcal{I}$ indicates that the vector was derived using time differentiation with respect to the inertial frame.

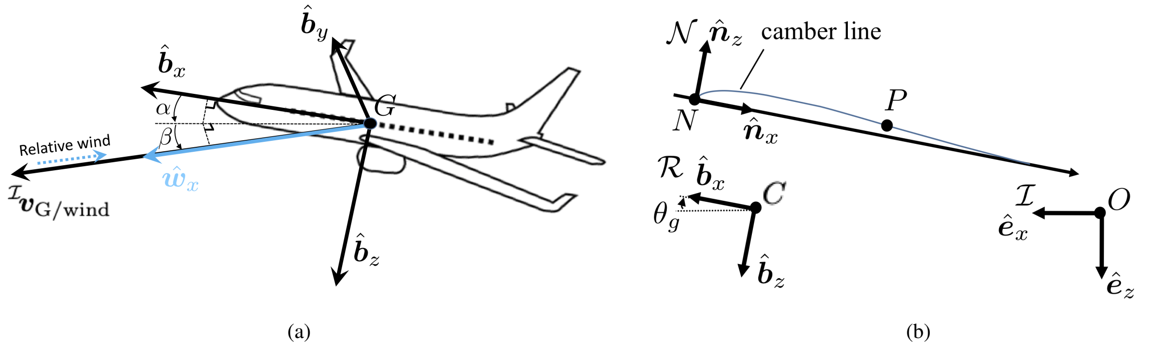

Fig. 2 a) Aircraft flight dynamics conventions for the body frame and the wind frame. b) Thin airfoil geometry and relevant reference frames.

Using the body frame $\mathcal{B}$, the relative velocity components can be expressed as [23]

$$[{}^{\mathcal{I}}\boldsymbol{v}_{\mathrm{G/flow}}]_B = \begin{bmatrix} u' \\ v' \\ w' \end{bmatrix}_{\mathcal{B}} = \begin{bmatrix} u \\ v \\ w \end{bmatrix}_{\mathcal{B}} - \begin{bmatrix} u_{\mathrm{flow}} \\ v_{\mathrm{flow}} \\ w_{\mathrm{flow}} \end{bmatrix}_{\mathcal{B}}, \tag{24}$$

where u, v, and w are the aircraft's velocity components and u_{flow}, v_{flow}, and w_{flow} are the freestream wind components. The notation $[\boldsymbol{v}]_{\mathcal{B}}$ indicates that the array entries are components of the vector $\boldsymbol{v}$ expressed in frame $\mathcal{B}$.

Based on the geometry shown in Fig. 2(a), the angle of attack is given by the components of (24) as [23]

$$\alpha = \tan^{-1}\left(\frac{w'}{u'}\right) = \tan^{-1}\left(\frac{w - w_{\mathrm{flow}}}{u - u_{\mathrm{flow}}}\right). \tag{25}$$

The angle of attack (25) includes both the motion of the vehicle and the freestream air flow. This expression applies at the center of mass G of the aircraft and is useful in deriving the aircraft's equations of motion using Euler's first law for rigid body motion, in which the aircraft is abstracted as a point mass located at the center of mass. In the following, the point-wise applicability of (25) enables application at individual points along the camber line of an airfoil to produce a local angle of attack at each point on the camber line. If the air is quiescent or the wind components are known from a model or measurements, only determining the u and w components of the inertial velocity in (25) is needed. The u_{flow} and w_{flow} components may come from impinging flow due to wind or represent flow components from wake effects, downwash/upwash, or induced flow from nearby coherent flow structures.

To derive the kinematics of a point along the mean camber line of an airfoil, consider a thin airfoil that can be represented by its mean camber line in Fig. 2(b). Figure 2(b) presents reference frames that are relevant to the construction of the kinematics. Let $\mathcal{R} = (C, \hat{\boldsymbol{b}}_x, \hat{\boldsymbol{b}}_y, \hat{\boldsymbol{b}}_z)$ be a reference frame that translates and rotates with the airfoil and is located at point C, which is the center of rotation for pitching maneuvers. Frame $\mathcal{R}$ is aligned with the body frame $\mathcal{B}$ of the vehicle but the center of rotation C may be offset from the center of mass G. The orientations of frames $\mathcal{R}$ and $\mathcal{I}$ match the common convention in aircraft flight dynamics, in which the body-x direction extends out of the nose of the aircraft and the body-z direction extends downward from the fuselage. For convenience, we also define reference frame $\mathcal{N} = (N, \hat{\boldsymbol{n}}_x, \hat{\boldsymbol{n}}_y, \hat{\boldsymbol{n}}_z)$ located at point N, which is the nose of the airfoil. The orientation of frame $\mathcal{N}$ matches the orientation often used in the aerodynamics literature (e.g., see [1, 8]), although it is sometimes located at the midchord (e.g., see [12]).

Let $\boldsymbol{r}_{P/O}$ be the position of an arbitrary point P on the camber line of the airfoil relative to point O. Finding the inertial velocity of point P so that we can replace point G with point P in (23) and (24) for calculation of a local angle of attack at point P using (25). Vector addition gives the position of point P relative to point O

$$\boldsymbol{r}_{P/O} = \boldsymbol{r}_{C/O} + \boldsymbol{r}_{P/C}, \tag{26}$$

where point C is the center of rotation for pitching maneuvers. Taking the inertial time derivative of (26) gives the inertial velocity of point P

$$ {}^{\mathcal{I}}\boldsymbol{v}_{P/O} = {}^{\mathcal{I}}\boldsymbol{v}_{C/O} + {}^{\mathcal{I}}\boldsymbol{v}_{P/C}. \tag{27}$$

The vector ${}^{\mathcal{I}}\boldsymbol{v}_{C/O}$ is the inertial velocity of the pitching center C, and ${}^{\mathcal{I}}\boldsymbol{v}_{P/C}$ velocity of point P relative to point C. Since frame $\mathcal{R}$ rotates with respect to frame $\mathcal{I}$ with angular velocity ${}^{\mathcal{I}}\boldsymbol{\omega}^{\mathcal{R}}$, the Transport Equation [22]

$$ {}^{\mathcal{I}}\boldsymbol{v}_{P/C} = {}^{\mathcal{R}}\boldsymbol{v}_{P/C} + {}^{\mathcal{I}}\boldsymbol{\omega}^{\mathcal{R}} \times \boldsymbol{r}_{P/C}, \tag{28} $$

is needed to differentiate $\boldsymbol{r}_{P/C}$. Note that ${}^{\mathcal{R}}\boldsymbol{v}_{P/C}$, which is the time rate of change of the vector $\boldsymbol{r}_{P/C}$ in frame $\mathcal{R}$, is zero since point P is stationary in $\mathcal{R}$. Since many thin-airfoil theory calculations occur in frame $\mathcal{N}$, consider the positions of points C relative to point N. From the geometry shown in Fig. 2(b), the position vector $\boldsymbol{r}_{P/C}$ can be written as

$$ \boldsymbol{r}_{P/C} = \boldsymbol{r}_{P/N} - \boldsymbol{r}_{C/N}. \tag{29} $$

Collecting (29), (27), and (28) provides the inertial velocity of the point P as

$$ {}^{\mathcal{I}}\boldsymbol{v}_{P/O} = {}^{\mathcal{I}}\boldsymbol{v}_{C/O} + {}^{\mathcal{I}}\boldsymbol{\omega}^{\mathcal{R}} \times \left(\boldsymbol{r}_{P/N} - \boldsymbol{r}_{C/N}\right). \tag{30} $$

To select coordinates, let the coordinates of $\boldsymbol{r}_{P/N}$ expressed in frame $\mathcal{N}$ be (x, z) and the coordinates of $\boldsymbol{r}_{C/N}$ expressed in frame $\mathcal{N}$ be (x_C, z_C). The vector $\boldsymbol{r}_{P/C}$ can be written in coordinates as

$$ \left(\boldsymbol{r}_{P/N} - \boldsymbol{r}_{C/N}\right) = (x - x_C)\,\hat{\boldsymbol{n}}_x + (z - z_C)\,\hat{\boldsymbol{n}}_z. \tag{31} $$

Also let (s, h) be the coordinates of $\boldsymbol{r}_{C/O}$ expressed in frame $\mathcal{I}$ so that $\boldsymbol{r}_{C/O} = s\hat{\boldsymbol{e}}_x + h\hat{\boldsymbol{e}}_z$ and the inertial velocity of the point C relative to O is ${}^{\mathcal{I}}\boldsymbol{v}_{C/O} = \dot{s}\hat{\boldsymbol{e}}_x + \dot{h}\hat{\boldsymbol{e}}_z$, where $\dot{s}$ and $\dot{h}$ represent the surge and plunge rates of the airfoil, respectively.

To calculate the angular velocity ${}^{\mathcal{I}}\boldsymbol{\omega}^{\mathcal{R}}$ in (28), examine the orientation of the airfoil. The chord line of the airfoil is oriented at an angle θ_g relative to frame $\mathcal{I}$. The angle θ_g is an Euler angle for the pitch orientation of the airfoil. We also sometimes refer to θ_g as a geometric angle of attack, since it corresponds with the angle of attack from traditional wind-tunnel testing for a non-maneuvering airfoil in the presence of a freestream flow in the $-e_x$ direction. The local angle of attack is formally specified by (25) and involves the freestream wind components as well as the motion of the airfoil. The pitch rate is $\dot{\theta}_g$, so the angular velocity becomes ${}^{\mathcal{I}}\boldsymbol{\omega}^{\mathcal{R}} = \dot{\theta}_g\hat{\boldsymbol{e}}_y = \dot{\theta}_g\hat{\boldsymbol{b}}_y$.

Substituting ${}^{\mathcal{I}}\boldsymbol{\omega}^{\mathcal{R}}$ into (30), the inertial velocity of point P becomes

$$ \begin{aligned} {}^{\mathcal{I}}\boldsymbol{v}_{P/O} &= {}^{\mathcal{I}}\boldsymbol{v}_{C/O} + \dot{\theta}_g\hat{\boldsymbol{b}}_y \times \left[-(x - x_C)\,\hat{\boldsymbol{b}}_x - (z - z_C)\,\hat{\boldsymbol{b}}_z\right], \\ &= \dot{s}\hat{\boldsymbol{e}}_x + \dot{h}\hat{\boldsymbol{e}}_z - \dot{\theta}_g\,(z - z_C)\,\hat{\boldsymbol{b}}_x + \dot{\theta}_g\,(x - x_C)\,\hat{\boldsymbol{b}}_z. \end{aligned} $$

Transforming the inertial unit vectors using $\hat{\boldsymbol{e}}_x = \cos\theta_g\hat{\boldsymbol{b}}_x + \sin\theta_g\hat{\boldsymbol{b}}_z$ and $\hat{\boldsymbol{e}}_z = -\sin\theta_g\hat{\boldsymbol{b}}_x + \cos\theta_g\hat{\boldsymbol{b}}_z$ provides

$$ {}^{\mathcal{I}}\boldsymbol{v}_{P/O} = \left[\dot{s}\cos\theta_g - \dot{h}\sin\theta_g - \dot{\theta}_g\,(z - z_C)\right]\hat{\boldsymbol{b}}_x + \left[\dot{s}\sin\theta_g + \dot{h}\cos\theta_g + \dot{\theta}_g\,(x - x_C)\right]\hat{\boldsymbol{b}}_z, \tag{32} $$

which is the inertial velocity of point P due to the two-dimensional kinematic motions of pitching at a rate of $\dot{\theta}_g$ about point C, plunging at a rate of $\dot{h}$, and surging at a rate of $\dot{s}$. Replacing G with P in (23) (and allowing for the slight abuse of notation in which (u', w') now represent the velocity components of point P instead of point G), the relative velocity components become

$$ u' = \dot{s}\cos\theta_g - \dot{h}\sin\theta_g - \dot{\theta}_g\,(z - z_C) - u_{\text{flow}}, \tag{33} $$

$$ w' = \dot{s}\sin\theta_g + \dot{h}\cos\theta_g + \dot{\theta}_g\,(x - x_C) - w_{\text{flow}}. \tag{34} $$

If convenient, the components $(u_{\text{flow}}, w_{\text{flow}})$ of the external flow vector ${}^{\mathcal{I}}\boldsymbol{v}_{\text{flow/O}}$ may be written in terms of the inertial-frame components (u_x, u_z) so that

$$ u_{\text{flow}} = u_x\cos\theta_g - u_z\sin\theta_g, \tag{35} $$

$$ w_{\text{flow}} = u_x\sin\theta_g + u_z\cos\theta_g. \tag{36} $$

Many aerodynamic calculations from thin-airfoil theory are performed in frame $\mathcal{N}$ instead of frame $\mathcal{B}$. Moreover, the relative velocity ${}^{\mathcal{I}}\boldsymbol{v}_{\text{flow/P}}$ is often considered instead of the ${}^{\mathcal{I}}\boldsymbol{v}_{\text{P/flow}}$, which is used in the construction of (25). However, the relationship

$$ \left[{}^{\mathcal{I}}\boldsymbol{v}_{\text{P/flow}}\right]_{\mathcal{B}} = \left[{}^{\mathcal{I}}\boldsymbol{v}_{\text{flow/P}}\right]_{\mathcal{N}} = \begin{bmatrix} u' \\ w' \end{bmatrix}_{\mathcal{N}}, \tag{37} $$

shows that (u', w') are the pertinent relative velocity components for the calculation of the local angle of attack in either convention. Plugging the u' and w' components from (33) and (34) into (25) yields the local angle of attack

$$\alpha = \tan^{-1}\left(\frac{\dot{s}\sin\theta_g + \dot{h}\cos\theta_g + \dot{\theta}_g\,(x - x_C) - w_{\text{flow}}}{\dot{s}\cos\theta_g - \dot{h}\sin\theta_g - \dot{\theta}_g\,(z - z_C) - u_{\text{flow}}}\right), \tag{38}$$

which applies to an arbitrary point P on the camber line of a maneuvering airfoil in a nonuniform freestream.

V. A New Expression for the Effective Angle of Attack of an Airfoil

This section derives a new expression for effective angle of attack that does not require the calculation of virtual camber. The new expression includes pitch, plunge, and surge motions of the airfoil, as well as freestream nonuniformity.

From thin-airfoil theory, the induced velocity component in the $\hat{\boldsymbol{n}}_z$ direction is given by (6) and the change of variables (8) as

$$w_{\text{in}}(\theta_0) = -\frac{1}{2\pi}\int_0^{\pi}\frac{\gamma(\theta)\sin\theta d\theta}{(\cos\theta - \cos\theta_0)}. \tag{39}$$

Using $w_{\text{in}} \approx w_{\text{in,n}}$ and $w_{\text{in,n}} = -V_{\infty,\text{n}}$ changes the expression to be in terms of the normal, freestream velocity component

$$V_{\infty,\text{n}}(\theta_0) = \frac{1}{2\pi}\int_0^{\pi}\frac{\gamma(\theta)\sin\theta d\theta}{(\cos\theta - \cos\theta_0)}. \tag{40}$$

The derivation in Section III proceeds by assuming a functional form of the circulation distribution $\gamma(\theta)$ to satisfy (40). A key observation that allows for the removal of the small-angle and small-camber-slope assumptions is that the form of the circulation distribution that solves the integral equation (40) is unrelated to the small-angle and small-camber-slope assumptions made on the left-hand-side of (9). However, note that the small-camber-slope assumption still partially remains implicitly in the small-camber assumption that projects the vortex sheet located on the x-axis. Even though these assumptions and the form of $\gamma(\theta)$ are often presented concurrently in the thin-airfoil theory derivation (e.g., see [1]), circulation distribution (10) solves the integral equation (40) to yield a cosine-series representation of $V_{\infty,\text{n}}(\theta_0)$ without requiring simplifications of $V_{\infty,\text{n}}(\theta_0)$. This observation is widely known and has previously been utilized by several authors (e.g., see [12, 14, 24–26].)

The circulation distribution (10) in thin-airfoil theory corresponds to a cosine-series representation of the flow impinging normal to the camber line

$$V_{\infty,\text{n}}(\theta) = V_\infty\left(A_0 - \sum_{n=1}^{\infty} A_n \cos\, n\theta\right), \tag{41}$$

which is found by inserting the circulation distribution (10) into the right-hand side of (40) and allowing the specific θ_0 to be a general θ location. Under a different convention of the angular coordinate and Fourier coefficients, such that $\phi = \theta - \pi$ and $\gamma_n = V_\infty A_n$, the authors in [12] compactly represent the right-hand side of (41) as the cosine-series $\sum_{n=0}^{\infty}\gamma_n\cos(n\phi)$. Since the freestream flow can be spatially nonuniform and the airfoil freely maneuvers, we replace the symbol $V_{\infty,\text{n}}$ by V_{n} to reflect the fact that the freestream is less well-defined. $V_{\text{n}}(\theta)$ represents the local, relative flow component that is normal to the camber line at the location θ. A constant, characteristic speed is also needed for nondimensionalization. Let $\overline{V}$ be a constant, characteristic speed associated with the problem, such as the steady speed of a moving airfoil or a spatially averaged wind speed for a stationary airfoil in an nonuniform flow. Define $\overline{V}_{\text{n}}(\theta) = V_{\text{n}}(\theta)/\overline{V}$ to be the nondimensional flow component impinging perpendicular to the camber line. This nondimensionalization ensures that the Fourier coefficients are also nondimensional, and (41) becomes

$$V_{\text{n}}(\theta) = \overline{V}\left(A_0 - \sum_{n=1}^{\infty} A_n \cos\, n\theta\right). \tag{42}$$

Utilizing the cosine-series representation of $V_{\text{n}}(\theta)$ in (42) and evaluating it at a specific θ_0 location, we re-perform the thin-airfoil theory derivation and express the Fourier coefficients and effective angle of attack in terms of $\overline{V}_{\text{n}}$. The condition of no flow across the camber line leads to the integral equation

$$\overline{V}\left(A_0 - \sum_{n=1}^{\infty} A_n \cos\, n\theta_0\right) = \frac{1}{2\pi}\int_0^{\pi}\frac{\gamma(\theta)\sin\theta d\theta}{(\cos\theta - \cos\theta_0)}. \tag{43}$$

The circulation distribution $\gamma(\theta)$ takes the same form as (10), except $\overline{V}$ replaces V_∞, so that

$$\gamma(\theta) = 2\overline{V}\left(A_0\frac{1+\cos\theta}{\sin\theta} + \sum_{n=1}^{\infty} A_n \sin\, n\theta\right). \tag{44}$$

Note that the form of the $\gamma(\theta)$ distribution in 44 retains the Kutta condition $\gamma(\pi) = 0$ from the classical thin-airfoil theory. Substitution verifies that (44) satisfies the integral equation (43). Fourier analysis provides the Fourier coefficients through (14) and (15), which become

$$A_0 = \frac{1}{\pi}\int_0^{\pi} \overline{V}_{\mathrm{n}}(\theta_0)d\theta_0, \tag{45}$$

$$A_n = -\frac{2}{\pi}\int_0^{\pi} \overline{V}_{\mathrm{n}}(\theta_0)\cos\, n\theta_0 d\theta_0. \tag{46}$$

Since the effective angle of attack given in terms of the Fourier coefficients in (20) remains unchanged by the choices made in this section, substitution of (45) and (46) into (20) provides the effective angle of attack

$$\alpha_{\mathrm{eff}} = -\frac{1}{\pi}\int_0^{\pi} \overline{V}_{\mathrm{n}}(\theta_0)(\cos\theta_0 - 1)d\theta_0. \tag{47}$$

The geometry shown in Fig. 1(b) can be used to obtain an expression for $\overline{V}_{\mathrm{n}}(\theta_0)$. Replacing V_∞ with $\|{}^{\mathcal{I}}\boldsymbol{v}_{\mathrm{flow/P}}\|$ and inserting the local angle of attack expression (25) into (3) yields

$$\overline{V}_{\mathrm{n}} = \frac{\sqrt{(u')^2 + (w')^2}}{\overline{V}} \sin\left[\tan^{-1}\left(\frac{w'}{u'}\right) + \tan^{-1}\left(-\frac{dz}{dx}\right)\right]. \tag{48}$$

Invoking the trigonometric identity

$$\sin(\tilde{\theta}_1 - \tilde{\theta}_2) = \sin\tilde{\theta}_1\cos\tilde{\theta}_2 - \cos\tilde{\theta}_1\sin\tilde{\theta}_2, \tag{49}$$

transforms (48) into

$$\sin\left[\tan^{-1}\left(\frac{w'}{u'}\right) + \tan^{-1}\left(-\frac{dz}{dx}\right)\right] = \sin\left(\tan^{-1}\left(\frac{w'}{u'}\right)\right)\cos\left(\tan^{-1}\left(\frac{dz}{dx}\right)\right) - \cos\left(\tan^{-1}\left(\frac{w'}{u'}\right)\right)\sin\left(\tan^{-1}\left(\frac{dz}{dx}\right)\right).$$

Note that the derivation in Section III retains the angle of attack α, however, invoking the local angle of attack (25) replaces α with a term that contains flow components (u', w') evaluated at that location. The presence of the arctangent function that results from the use of the local angle of attack (25) enables use of the additional trigonometric identities,

$$\sin\left(\tan^{-1}\tilde{\theta}\right) = \frac{\tilde{\theta}}{\sqrt{1+\tilde{\theta}^2}}, \quad \text{and} \quad \cos\left(\tan^{-1}\tilde{\theta}\right) = \frac{1}{\sqrt{1+\tilde{\theta}^2}}, \tag{50}$$

which leads to

$$\overline{V}_{\mathrm{n}} = \sqrt{(u')^2 + (w')^2}\frac{\frac{w'}{u'} - \frac{dz}{dx}}{\overline{V}\sqrt{\left(1+\left(\frac{w'}{u'}\right)^2\right)\left(1+\left(\frac{dz}{dx}\right)^2\right)}}. \tag{51}$$

Under the mild assumption that $u' > 0$ (to avoid having to consider a $\mathrm{sgn}(u')$ term), (51) can be rewritten as

$$\overline{V}_{\mathrm{n}} = \frac{w' - u'\frac{dz}{dx}}{\overline{V}\sqrt{1+\left(\frac{dz}{dx}\right)^2}}. \tag{52}$$

For flows in which u' changes sign (e.g., pulsatile flow), the $\mathrm{sgn}(u')$ term must be maintained. Using (52) to eliminate $\overline{V}_{\mathrm{n}}$ from (47) leads to a new expression for effective angle of attack,

$$\boxed{\alpha_{\mathrm{eff}} = -\frac{1}{\pi}\int_0^{\pi} \frac{w' - u'\frac{dz}{dx}}{\overline{V}\sqrt{1+\left(\frac{dz}{dx}\right)^2}}\left(\cos\theta_0 - 1\right)d\theta_0,} \tag{53}$$

where

$$u'(\theta_0) = (\dot{s} - u_x)\cos\theta_g - (\dot{h} - u_z)\sin\theta_g - \dot{\theta}_g\left(z(\theta_0) - z_C\right), \tag{54}$$

$$w'(\theta_0) = (\dot{s} - u_x)\sin\theta_g + (\dot{h} - u_z)\cos\theta_g + \dot{\theta}_g\left(\frac{c}{2}(1 - \cos\theta_0) - x_C\right). \tag{55}$$

Equations (54) and (55) are based on the relative flow components (33) and (34) after expressing the wind components in the inertial frame and using the change of variables (8). The freestream components u_x and u_z may also be functions of θ_0 if there is spatial nonuniformity in the surrounding flowfield.

The use of the Kutta-Joukowski theorem [1] in the creation of the α_{eff} definition (20) limits (53) to spatially nonuniform flows that are potential (i.e., irrotational) flows, since potential flow is used for the derivation of this theorem. If the freestream flow has distributed vorticity, a flow velocity function can still be used to calculate an effective angle of attack using (53), subject to the assumption of a Kutta-Joukowski relation between sectional lift and bound circulation. Equations (53)-(55) are important because they provide a simple formula for calculating effective angle of attack under various flow conditions and kinematics. Reducing the small-angle and small-camber-slope assumptions has also allowed more terms to be maintained. Using (50), the $1/\sqrt{1 + (dz/dx)^2}$ term is often well approximated by 1 in many applications. However, the pitch axis location (x_c, z_c) in u' and w' may play an important role in applications where these values are large. For example, although it is not examined in this paper, the $u'\,(dz/dx)$ term may increase in importance for vertical-axis wind turbine applications in which z_c is large.

VI. Special Cases

This section examines implications of the proposed effective angle of attack expression for several applications, including a maneuvering symmetric airfoil, a thin airfoil encountering a transverse flow, and a cambered airfoil in steady, uniform flow. In addition to showing that the proposed expression (53) properly encompasses the prior effective angle of attack expression (22), this section presents a new expression for the zero-lift angle of attack for a cambered thin airfoil that replaces the classical expression.

A. Effective Angle of Attack for Maneuvering Symmetric Airfoil

We consider whether the proposed expression for effective angle of attack (53) properly encompasses the previous effective angle of attack expression (22) for a pitching and plunging thin airfoil under the appropriate simplifying assumptions. The example in [8] (see pg. 430) considers a thin airfoil without camber (i.e., $dz/dx = 0$) in a freestream of flow speed $\overline{V} = V_\infty$. Plugging into (53) leads to

$$\alpha_{\text{eff}} = -\frac{1}{\pi}\int_0^\pi \frac{w'}{V_\infty}(\cos\theta_0 - 1)\,d\theta_0. \tag{56}$$

The derivation of (22) also considers the relative velocity between the airfoil motion and the freestream, so we may assume that incident wind is in the inertial $\hat{\boldsymbol{e}}_x$ direction with $u_x = -V_\infty$ and the airfoil is not surging forward (i.e., $\dot{s} = 0$). The thin airfoil has a geometric angle of attack $\theta_g = \alpha$ and pitches at a rate of $\dot{\theta}_g = \dot{\alpha}$ about a point on the chord line located at $(x_C, z_C) = (b + ab, 0)$. The airfoil has a plunge rate of $\dot{h}$. Plugging these expressions into (53) — (55), and using $c = 2b$ gives

$$\alpha_{\text{eff}} = -\frac{1}{\pi}\frac{V_\infty\sin\alpha + \dot{h}\cos\alpha - \dot{\alpha}(b + ab)}{V_\infty}\int_0^\pi(\cos\theta_0 - 1)\,d\theta_0 + \frac{\dot{\alpha}b}{\pi V_\infty}\int_0^\pi(\cos\theta_0 - 1)^2\,d\theta_0. \tag{57}$$

The two integrals shown in (57) can be evaluated analytically to yield $-\pi$ and $3\pi/2$, from left to right, respectively. Continued calculation reduces the effective angle of attack to

$$\alpha_{\text{eff}} = \sin\alpha + \frac{\dot{h}}{V_\infty}\cos\alpha + b\left(\frac{1}{2} - a\right)\frac{\dot{\alpha}}{V_\infty}. \tag{58}$$

Equation (58) is the effective angle of attack for a flat, thin airfoil pitching about ab and plunging at a rate of $\dot{h}$. The first term is a geometric angle of attack contribution. The second term is a plunge-rate contribution, and the third term is a pitch-rate contribution. Note that if the small angle assumption is applied, so that $\sin\alpha \approx \alpha$ and $\cos\alpha \approx 1$, (58) successfully recovers the traditional effective angle of attack expression (22).

B. Angle of Attack Contribution for Transverse Flow

Consider the scenario of a flat plate or symmetric airfoil (i.e. $dz/dx = 0$) in a steady freestream, at a constant geometric angle of attack, and encountering a transverse flow (e.g., see [9]). The need to incorporate the effect of a transverse flow in an angle of attack calculation often occurs in rotorcraft research, in which rotor blades experience downwash [12] or in fixed-wing flight applications in the presence of three-dimensional effects, such as wing-tip vortices [1]. A common practice is to add a local angle of attack contribution $\tan^{-1}(w/V_\infty)$ due to the transverse flow component w to the geometric angle of attack, yielding [9]

$$\alpha_{\text{eff}} = \theta_g + \tan^{-1}\left(\frac{w}{V_\infty}\right). \tag{59}$$

Peters et al. [12] note that although (59) is commonly implemented, it is known to be incorrect, because at zero geometric angle of attack, the lift should be proportional to $2\pi\rho b V_\infty^2 (w/V_\infty)$, not $2\pi\rho b V_\infty^2 \tan^{-1}(w/V_\infty)$.

Let the freestream be $u_x = -V_\infty$ and take $\overline{V} = V_\infty$. For this problem, we have $\dot{s} = \dot{h} = \dot{\theta}_g = 0$. If the transverse flow component u_z is evaluated at a single, representative location, then substitution into (53) leads to

$$\alpha_{\text{eff}} = \sin\theta_g - \frac{u_z}{V_\infty}\cos\theta_g. \tag{60}$$

Equation (60) is a corrected version of (59), where $w = -u_z\cos\theta_g$ due to the change of reference frames. The transverse-flow contribution to α_{eff} is (w/V_∞), not $\tan^{-1}(w/V_\infty)$, which agrees with the remark of Peters et al. [12].

C. Zero-Lift Angle for a Thin Airfoil

Consider the steady flow past a thin airfoil with the slope of the camber line dz/dx at a fixed geometric angle of attack θ_g in a uniform freestream in the horizontal direction. The zero-lift angle from thin-airfoil theory is [1]

$$\alpha_{l=0} = -\frac{1}{\pi}\int_0^\pi \frac{dz}{dx}(\cos\theta_0 - 1)\,d\theta_0. \tag{61}$$

We find the zero-lift angle for the present theory by setting $C_l = 2\pi\alpha_{\text{eff}} = 0$, where α_{eff} is specified by (53). We also set $u_x = -V_\infty$ and $u_z = \dot{s} = \dot{h} = \dot{\theta}_g = 0$ and solve for the geometric angle of attack θ_g at zero lift

$$\theta_{g,l=0} = \tan^{-1}\left(\frac{\int_0^\pi \sin\left(\tan^{-1}\left(\frac{dz}{dx}\right)\right)(\cos\theta_0 - 1)\,d\theta_0}{\int_0^\pi \cos\left(\tan^{-1}\left(\frac{dz}{dx}\right)\right)(\cos\theta_0 - 1)\,d\theta_0}\right). \tag{62}$$

Note that (62) does not readily simplify since the slope of the camber line dz/dx is a function of the variable of integration θ_0. Equation (62) replaces the classical result for the zero-lift angle (61).

For a more accessible comparison to existing results from thin-airfoil theory, consider instead the value of the lift coefficient at zero geometric angle of attack. Substituting $\theta_g = 0$ into $C_l = 2\pi\alpha_{\text{eff}}$, where α_{eff} is specified by (53) results in

$$C_l(\theta_g = 0) = 2\pi\left[-\frac{1}{\pi}\int_0^\pi \sin\left(\tan^{-1}\left(\frac{dz}{dx}\right)\right)(\cos\theta_0 - 1)\,d\theta_0\right]. \tag{63}$$

Equation (63) is directly comparable to the result from thin-airfoil theory that can be obtained by inserting (61) into $C_l = 2\pi(\alpha - \alpha_{l=0})$ for $\alpha = 0$. From this comparison, the two equations are identical under the approximation that

$$\sin\left(\tan^{-1}\left(\frac{dz}{dx}\right)\right) \approx \frac{dz}{dx}.$$

Equation (63) shows that the proposed theory of this paper encompasses the steady thin-airfoil theory results, but does so without explicitly invoking a small-camber-slope assumption.

Table 1 presents the results of a comparison of thin-airfoil theory in (61), the present theory in (62), and experimental data obtained from the literature in [27] for several four-digit NACA airfoils. The equations for the camber lines of the four-digit NACA airfoil series can be found in [28]. Table 1 does not included a comparison to the data of [12], because Peters et al. [12] include additional approximations related to the truncation of a Fourier series that must be fit to the

Table 1 Comparison of the zero-lift angle for four-digit NACA airfoils.

NACA airfoil	Thin-airfoil theory in (61) $\alpha_{l=0}$ (deg)	Proposed theory in (62) $\theta_{g,l=0}$ (deg)	Experiment in [27] $\alpha_{l=0}$ (deg) ±0.15 deg
0012	0.000	0.000	0.0
2412	-2.077	-2.076	-2.0
4412	-4.155	-4.142	-4.1
6412	-6.232	-6.191	-6.1
6712	-9.130	-8.787	-7.4
8318	-7.672	-7.636	-7.4

camber line of the airfoil— these approximations complicate the comparisons. However, we note that the proposed expression (62) has the advantage that it does not require fitting a Fourier series to the camber line prior to calculation.

For airfoils NACA 0012, 2412, 4412, and 6412, both theories offer predictions that lie within the estimated ±0.15 degree experimental uncertainty found in [27, 29]. For the NACA 2412 airfoil, there is very little difference between the theories. As the maximum camber grows and moves towards the tail of the airfoil, such as in the cases of the NACA 6412 and NACA 6712 airfoils, the difference between the estimates increases. The case of the NACA 6712 airfoil shows that if the location of maximum camber moves very far aft on the chord, both theories have difficulty predicting the true value.

The experimental uncertainty is too large to conclude that the proposed theory provides an improvement over the existing thin-airfoil theory. However, Table 1 shows that the proposed theory produces zero-lift angle estimates that are consistently smaller or equal in magnitude for all cases, which is a trend that is the direction of the experimental values. If an improvement exists, it should be noted that the magnitude of the improvement only accounts for a small portion of the difference between the existing theory and experiment, which is presumably attributable to modeling assumptions related to airfoil thickness and viscous effects.

VII. Effective Angle of Attack Matching

This section uses the proposed effective of attack expression for creation of a motion profile for a maneuvering airfoil to mimic a specified lift response. In particular, this section examines how to match the effective angles of attack for a non-maneuvering airfoil that encounters a small-amplitude, transverse gust and another, freely maneuvering airfoil that does not encounter a gust. A small-amplitude, transverse gust is defined similar to [30] to have a gust ratio GR ≤ 0.2. Gust encounters are an active area of unsteady aerodynamics research [18, 31]. However, creating experimental setups to study unsteady flow phenomena, such as gust encounters can be challenging [17]. Effective angle of attack matching provides a method for creating motion profiles to mimic or closely approximate an aerodynamic response.

Section VII.A presents a framework for choosing input signals to match a desired angle of attack. Section VII.B uses pitching or plunging inputs individually, and Section VII.C uses both pitching and plunging inputs.

A. Optimal Control Problem Description

Consider a NACA 2412 cambered airfoil traveling with constant, horizontal speed $\dot{s} = 0.4 m/s$ at a constant geometric angle of attack $\theta_{g,0} = 0°$ and encountering a transverse, sine-squared gust at $t = 0$. The transverse gust has a sine-squared velocity profile [9]

$$u_z(x,t) = \begin{cases} -V_{\max} \sin^2\left(\frac{\dot{s}t - x}{L}\pi\right) & \text{if} \quad 0 \leq \frac{\dot{s}t-x}{L} \leq 1, \\ 0 & \text{otherwise,} \end{cases} \tag{64}$$

where $V_{\max}$ is the maximum speed of the gust and L is the gust width. Note that the piecewise construction of this function permits the evaluation of the gust velocity along the chord if the location x is either inside or outside of the gust region. Consider also an airfoil that does not encounter a gust but tries to mimic the effect of the gust by pitching and plunging. The maneuvering airfoil has the same surge rate $\dot{s}$ and the same initial geometric angle of attack $\theta_{g,0}$. By letting $V_{\max} = 0.2\dot{s}$ and assuming a chord of $c = 0.1$ m, the simulated gust encounter corresponds to gust ratio $GR = V_{\max}/\dot{s} = 0.2$ at a chord-based Reynolds number of $Re_c \approx 2,660$ in air or $Re_c \approx 39,800$ in water.

Let $\alpha^{(1)}_{\text{eff}}$ and $\alpha^{(2)}_{\text{eff}}$ be the effective angles of attack for airfoils 1 and 2 respectively, where airfoil 1 encounters the gust and airfoil 2 does not. To perform matching of the effective angle of attack, we construct the following constrained optimization problem to find the optimal (open-loop) control input u that solves

$$\min_{u} \quad J(u) = \frac{1}{2}\int_{t_0}^{t_f} \left(\alpha_{\text{eff}}^{(1)}(t) - \alpha_{\text{eff}}^{(2)}\left(\theta_g, u\right)\right)^2 \mathrm{d}t \tag{65}$$

$$\begin{aligned} \text{subject to} \quad \dot{\theta}_g &= u_1, \quad \text{with} \;\; \theta_g(0) = \theta_{g,0}, \\ \dot{h} &= u_2, \quad \text{with} \;\; h(0) = 0. \end{aligned}$$

The control inputs u_1 and u_2 command the pitch rate $\dot{\theta}_g$ and plunge rate $\dot{h}$, respectively. The effective angle of attack for the gust encounter $\alpha_{\text{eff}}^{(1)}(t)$ is a function of time only since it can be calculated using the known gust profile. The $z(x)$ and dz/dx terms in α_{eff} correspond to the appropriate NACA airfoil equation for the mean camber line of a NACA 2412 airfoil, which can be found in [28]. The characteristic speed $\overline{V}$ for this problem is set to $\overline{V} = \sqrt{\dot{s}^2 + V_{\text{max}}^2}$. For the maneuvering airfoil, the effective angle of attack $\alpha_{\text{eff}}^{(2)}$ is a function of the airfoil motion variables θ_g, $\dot{\theta}_g$, and $\dot{h}$.

To solve the constrained optimal control problem (65) computationally, we assume a Fourier-series parameterization of the control inputs [32]

$$u_1(t) = C_0 + \sum_{n=1}^{N} C_{2n-1}\sin(n\omega t) + C_{2n}\cos(n\omega t), \tag{66}$$

$$u_2(t) = D_0 + \sum_{n=1}^{N} D_{2n-1}\sin(n\omega t) + D_{2n}\cos(n\omega t), \tag{67}$$

where $\omega = 2\pi/T$. The parameterizations in (66) and (67) restrict the spaces of possible solutions for $u_1(t)$ and $u_2(t)$ from an infinite-dimensional spaces of continuous curves on the interval $[0, T]$ to the finite-dimensional space of Fourier coefficients. That is, given the Fourier coefficients C_n and D_n for $n = 0, \ldots, 2N$, continuous curves $u_1(t)$ and $u_2(t)$ are completely specified on the interval $[0, T]$. Larger values of N allow for more complex curves. In the examples of this section, we select $N = 6$, since this value was found to provide adequate degrees of freedom to match the effective angles of attack. The coefficients C_0, and D_0 allow for constant offsets. For pre-specified controls $u_1(t)$, and $u_2(t)$, the differential equation constraints in (65) can be readily integrated and plugged into the cost function to eliminate the constraint, yielding an unconstrained problem. The unconstrained optimization problem is solved using the numerical optimization function `fminunc` in MATLAB® [33].

B. Effective Angle of Attack Matching with a Single Input

To examine the ability of a single input to match the effective angle of attack of a gust encounter, consider either pure pitching or pure plunging motion. For pure pitching motion, the plunging input is set to $u_2(t) = 0$ during the entire maneuver. Conversely, for pure plunging motion, the pitching input is set to $u_1(t) = 0$.

Given an initial guess of Fourier coefficients for the appropriate control input in either (66) or (67), the corresponding effective angle of attack for the pitching or plunging motion can be calculated and the optimization can be initiated. It was found that optimization solver occasionally converged to local minima, indicating that the optimization problem (65) is nonconvex. To address this problem, we considered various random values of initial guesses for the Fourier coefficients and separately solved the optimization problem from each initial guess. Across all solves considered, the solution with the lowest cost J was selected. For the pure pitching motion, with an initial guess of Fourier coefficients $C_0 = 0$, $C_1 = 0.0586$, and $C_n = 0$ for $n = 2, \ldots, 12$, the results of the optimization are shown in Fig. 3(a) and Fig. 3(b). This initial guess for the C_n Fourier coefficients resulted in accurate and indistinguishable matching of the α_{eff} curves, as shown in Fig. 3(a). The resulting control signal $u_1(t)$ is shown in Fig. 3(b) as a dashed red line and consists of a pitch-up, then pitch-down maneuver.

For the pure plunging motion with an initial guess of Fourier coefficients $D_0 = 0.0264$, $D_1 = 0$, $D_2 = -0.0264$, and $D_n = 0$ for $n = 3, \ldots, 12$, the results of the optimization are shown in Fig. 3(c) and Fig. 3(d). The optimization routine was able to closely match the α_{eff} curves, as shown in Fig. 3(c). The resulting control signal $u_2(t)$ is shown in Fig. 3(d) as a dashed red line and consists of a positive plunging maneuver. The optimal solution notably contained a nonzero Fourier coefficient D_0 to offset the plunging effect at the initial time. The control inputs in Fig. 3(c) and Fig. 3(d) illustrate a pitch-plunge equivalence, since either pure pitching or pure plunging motion can match the effective angle of attack of a small-amplitude, transverse gust encounter. However, the plunge input profile in Fig. 3(d) is notably

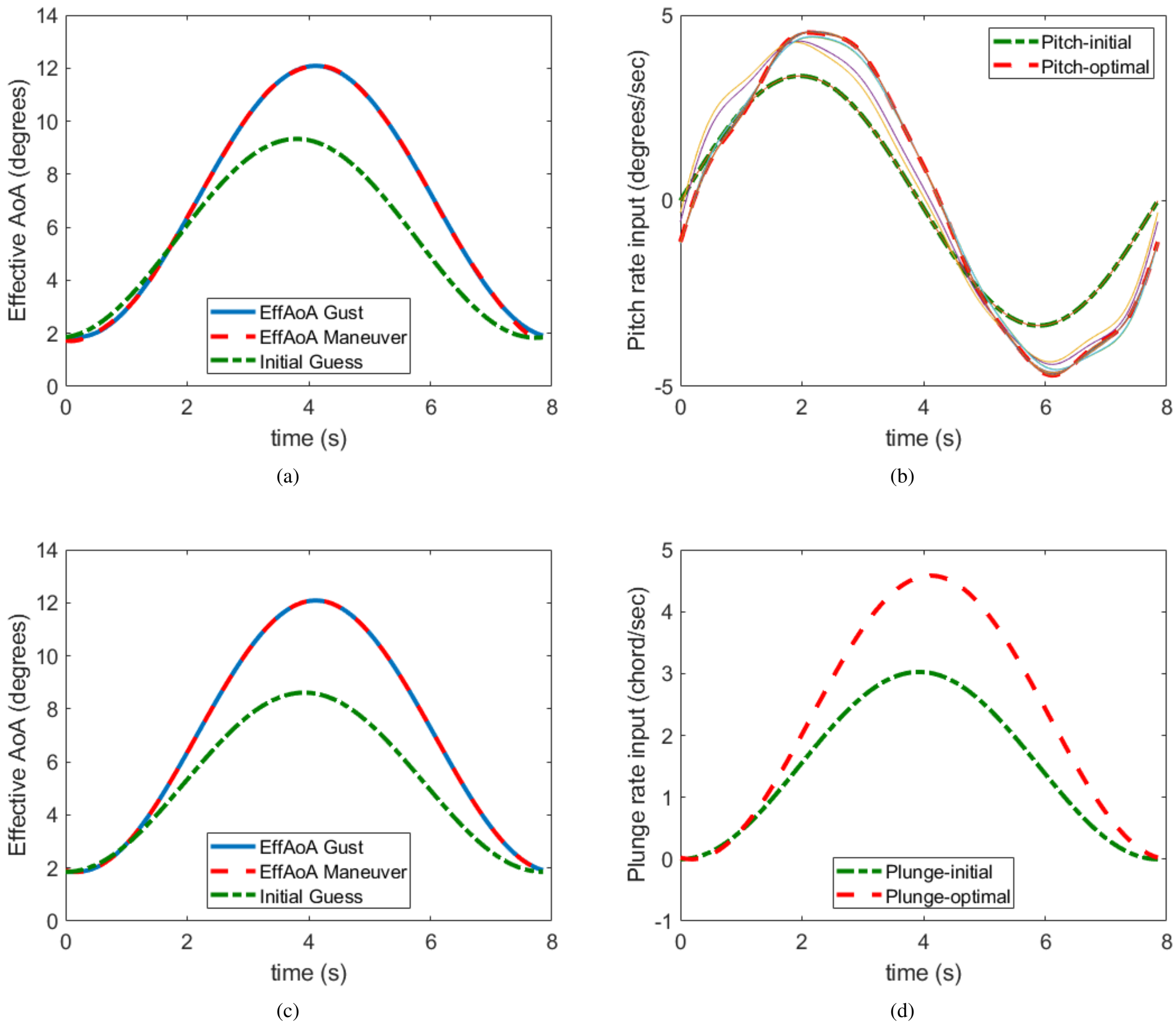

Fig. 3 Effective angles of attack for an airfoil encountering a gust and an airfoil mimicking a gust encounter through pitching only (Fig. 3a) and plunging only (Fig. 3c). Pitch rate initial guess, iterations (thin lines) and optimal profile (Fig. 3b). Plunge-rate initial guess and optimal profile (Fig. 3d).

smoother, suggesting that the plunging input is more well-suited for mimicking a small-amplitude, transverse gust encounter.

C. Effective Angle of Attack Matching for Combined Pitching and Plunging Inputs

This section examines the simultaneous design of pitching input $u_1(t)$ and plunging input $u_2(t)$. Using both control parameterizations (66) and (67) in the optimal control problem (65) leads control solutions that combine both pitching and plunging. Figure 4 shows the results of matching the effective angle of attack using combined pitching and plunging motions. Using several inputs, multiple solutions become possible. Figures 4(a) and 4(b) show that the results from one solution, and Figs. 4(c) and 4(d) show the results from another solution with different profiles for pitching and plunging.

The first solution was generated with an initial guess of Fourier coefficients $C_0 = 0$, $C_1 = 0.0168$, and $C_n = 0$ for $n = 2, \ldots, 12$, for $u_1(t)$, combined with an initial guess of Fourier coefficients $D_0 = 0.0264$, $D_1 = 0$, $D_2 = -0.0264$, and $D_n = 0$ for $n = 3, \ldots, 12$, for $u_2(t)$. The initial guess of the pitching and plunging inputs for the maneuvering airfoil resulted in a similar effective angle of attack profile in Fig. 4(a), so the optimal maneuvers in Fig. 4(b) are close to the inputs of the initial guess. The alternate solution shown in Figs. 4(c) and 4(d) was based on an initial guess of Fourier

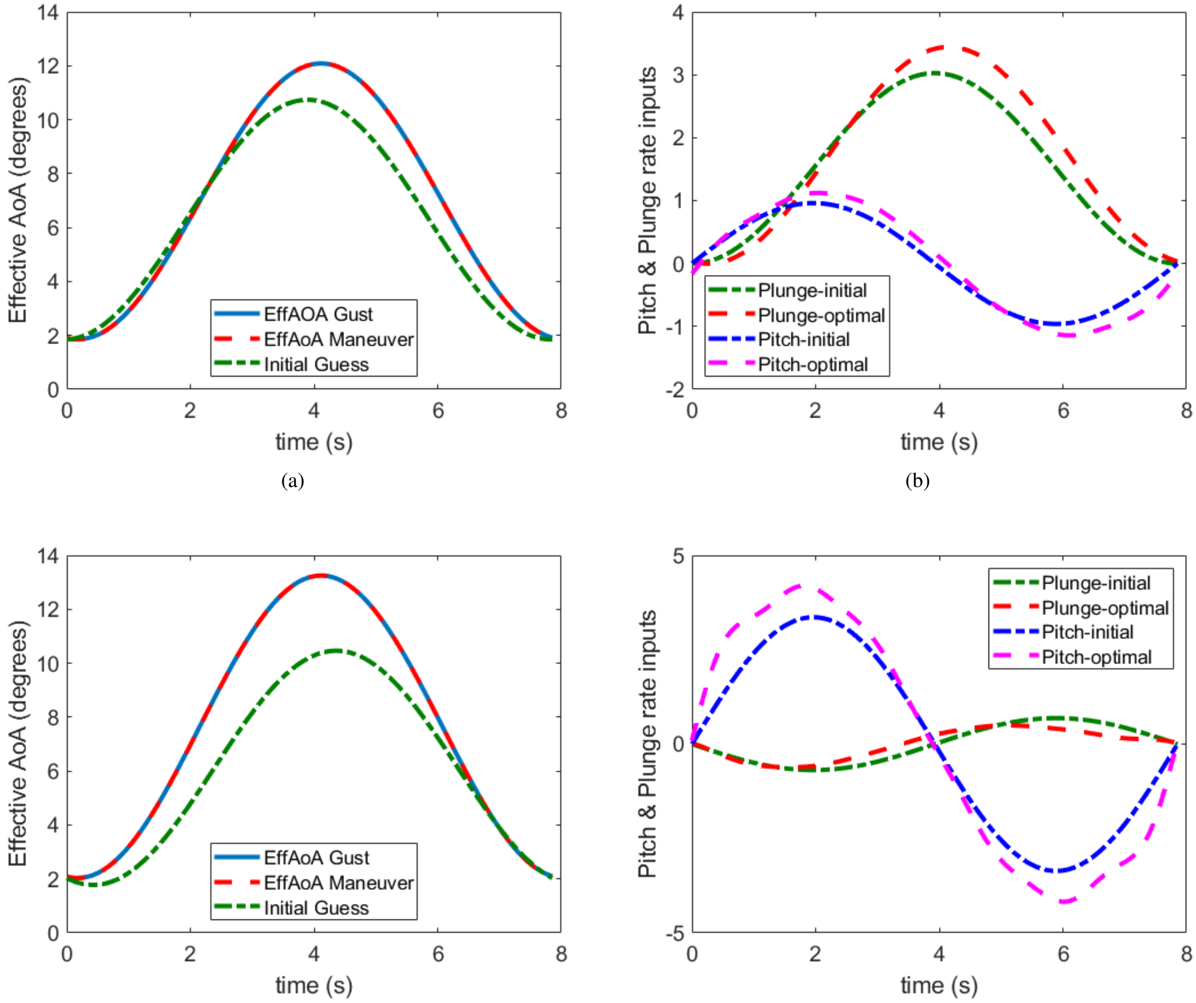

(a) (b) (c) (d)

Fig. 4 Effective angle of attack profiles from different initial guesses for an airfoil maneuvering to mimic a gust encounter through pitching and plunging (Fig. 4a and 4c). Rate inputs calculated by the matching optimization from different initial guesses (Fig. 4b and 4d).

coefficients $C_0 = 0$, $C_1 = 0.0586$, and $C_n = 0$ for $n = 2, \ldots, 12$, for $u_1(t)$, combined with an initial guess of Fourier coefficients $D_0 = 0$, $D_1 = -0.0120$, and $D_n = 0$ for $n = 2, \ldots, 12$, for $u_2(t)$. For this initial guess, the effective angle of attack did not match the desired effective angle of attack as closely in Fig. 4(c). However, the optimization solver was still able to find an input combination to match the effective angle of attack $\alpha_{\text{eff}}^{(1)}$ for the airfoil in a gust encounter. Fig. 4(b) shows optimal control inputs for a pitch-up then pitch-down maneuver, combined with a positive plunge maneuver. Fig. 4(d) provides another solution of optimal control inputs with a larger pitch-up then pitch-down maneuver, plus a small-amplitude plunging cycle. Notably, the first solution in Fig. 4(b) has more plunge actuation and is smoother, which is consistent with the findings of Section VII.B that slow plunging is well-suited to mimic a small-amplitude transverse gust. The second solution in Fig. 4(d) employs more pitching than plunging actuation. Even though an additional plunge input is present, Fig. 4(d) exhibits the same bumps in the pitching input curve that are present in Fig. 3(b) for a single pitching input.

The four solutions shown in this section for matching the effective angle of attack confirm that different kinematic motions can emulate the effective angle of attack in a transverse gust encounter, which implies the same lift response under a quasi-steady assumption. Although the effective angle of attack matching problem of this section is focused on

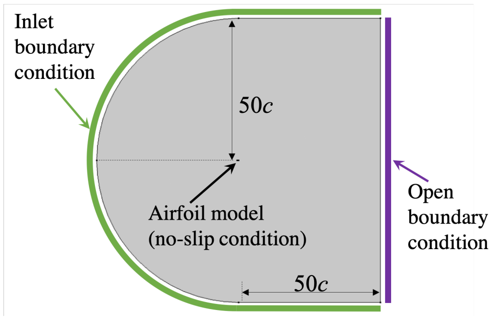

(a)

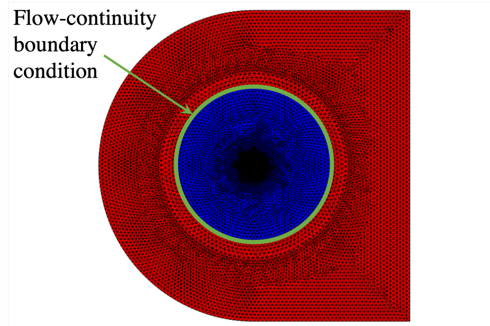

(b)

Fig. 5 Geometry and boundary conditions for CFD simulations. a) Configuration for the steady-flow and gust encounter simulations. b) Configuration and mesh for the pitching simulation.

emulation of a gust encounter, the provided framework that utilizes the proposed effective angle of attack expression (53) and the optimal control formulation (65) is applicable to various other problems of aerodynamic force equivalence. For example, there has been significant work on pitch-plunge equivalence (e.g., see [16]) as well as more general, three degree-of-freedom motions for gust encounter emulation (e.g., see [17]).

VIII. Computational Fluid Dynamics Simulations

This section presents CFD simulations that demonstrate the efficacy of the proposed effective angle of attack theory from Sections V and VI , as well as the effective angle of attack matching framework from Section VII. Steady-flow past several NACA airfoils was simulated. A gust encounter with a NACA 2412 airfoil was simulated, and a pitching maneuver designed to mimic a gust encounter was simulated for the same airfoil.

A. CFD methods

The commercially available software package COMSOL Multiphysics® v. 5.5 [34] was used to perform the two-dimensional simulations in this section. The simulation domain consisted of the union of a half-circle and a rectangle, as shown in Fig. 5(a). The fluid was assumed to be air at standard temperature and pressure. An airfoil model was drawn in the half-circle portion of the domain with the trailing-edge point coincident with the center of the semi-circle. Inlet, open, and no-slip boundary conditions were applied as shown in Fig. 5(a). For the steady-flow and gust encounter simulations, the airfoil remained in a horizontal orientation and the flow velocity was prescribed on the inlet boundary to achieve the desired angle of attack or to impose a transverse gust velocity. For the pitching simulation, a concentric circular domain was added in Fig. 5(b) to enclose the airfoil so that the mesh near the airfoil could be rotated independently from the surrounding domain without the need to re-mesh [35]. A flow-continuity boundary condition was applied on the circle, and the circular domain was rotated for the maneuver.

Steady-flow simulations were performed using a turbulent flow solver. The solver implements the Reynolds-Averaged Navier-Stokes (RANS) and continuity equations with a Shear Stress Transport (SST) turbulence model. Following [36], the freestream turbulent kinetic energy was set to $k_\infty = 0.1\nu_\infty\overline{V}/(50c)$, and the freestream specific dissipation rate was set to $\omega_\infty = 10\overline{V}/(50c)$ for the chord-based Reynolds number of $\mathrm{Re}_c = 6\times10^6$. The example simulation [36] provided by COMSOL Multiphysics® for flow past a NACA 0012 compares very well with the experimental data of [37]. For each airfoil considered in steady flow, the Reynolds number was set to $\mathrm{Re}_c = 6\times10^6$. In this regime, the lift vs. angle of attack curves are rather invariant to changes in the Reynolds number, and thin-airfoil theory is known to perform well.

Since a primary use of the angle of attack matching from Section VII is for the design of laboratory experiments to simulate gust encounters, the low Reynolds number $Re_c \approx 2,660$ in air was considered for the gust encounter and pitching simulations. A similar Reynolds number of $Re_c \approx 39,800$ in water can be achieved in a towing tank setup similar to [18], but this configuration is not examined here. Due to the Reynolds number, a laminar flow solver was selected in COMSOL Multiphysics®. The solver implements the Navier-Stokes equations and the continuity equation with an incompressibility constraint. For all simulations, mesh convergence was checked by sequentially reducing the physics-controlled mesh size option in COMSOL Multiphysics® and including additional boundary layer elements near

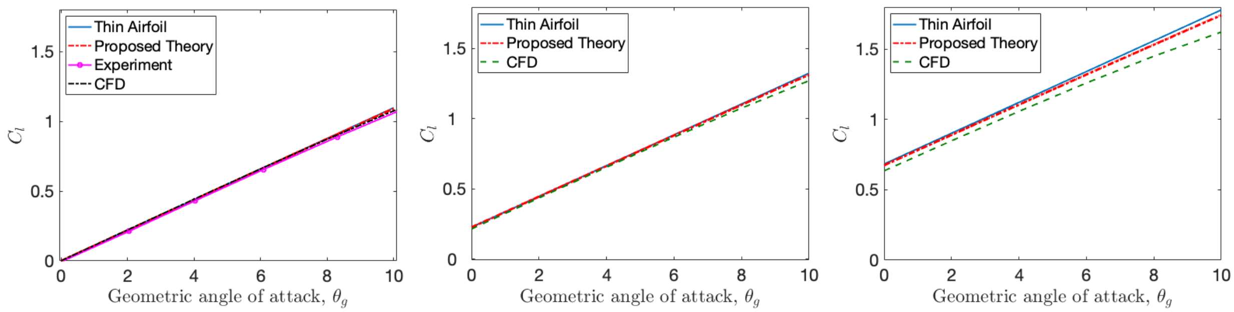

(a) NACA 0012 (b) NACA 2412 (c) NACA 6412

Fig. 6 Comparison of thin-airfoil theory, the proposed theory, and CFD simulation on plots of C_L vs. geometric angle of attack θ_g for steady flow at Re = 6×10^6 past airfoils: (a) NACA 0012, (b) NACA 2412, and (c) NACA 6412. Plot (a) contains experimental data from [37].

the surface of the airfoil as necessary until the lift curve plots did not change with mesh size.

B. CFD results for steady-flow simulations

Simulations were performed for steady-flow past NACA 0012, 2412, and 6412 airfoils to compare the coefficients of lift from the proposed theory to those obtained from thin-airfoil theory and CFD simulation. Figure 6 presents the results of these calculations. Similar to [36], Figure 6(a) contains the experimental data of Ladson [37] which very closely agrees with the theory and CFD simulations. Note that for the two cambered airfoils, NACA 2412 and 6412, the thin-airfoil theory curve based on (21) includes the effects of camber, leading to a lift offset at zero angle of attack. The NACA 2412 airfoil is used subsequently in this section in time-varying simulations for a gust encounter and a pitching maneuver. Due largely to the flow being attached at these angles of attack, all three methods give similar lift curves in each of the figures. For each airfoil, the proposed theory lies between the thin-airfoil prediction and the CFD curve, as clearly seen in the case of the highly cambered NACA 6412 airfoil. The proposed theory very modestly improves the steady-flow lift predictions of thin-airfoil theory. However, viscous affects and remaining thin-airfoil-theory assumptions may be responsible for the differences between the solutions from CFD and the proposed theory.

C. CFD results for effective angle of attack matching

To validate the effective angle of attack matching framework presented in Section VII, CFD simulations of a NACA 2412 airfoil encountering a transverse gust and a NACA 2412 airfoil pitching in a uniform flow were performed. Two-dimensional simulations were performed because a transverse gust encounter could be readily implemented in COMSOL Multiphysics® using a time-varying inlet boundary condition. The flow field during the entry period of a gust encounter (i.e., just prior to the lift peak) has been shown to be quasi-two-dimensional [30] for the same gust ratio simulated here (GR= 0.2). However, Grubb et al. [38] have shown for GR= 1.0, three-dimensional simulation is necessary to match experimental data. The results of this section validate the two-dimensional effective angle of attack theory of this paper; results do not capture three dimensional effects that may be important in a real gust encounter. The boundary condition implemented the sine-squared gust profile and parameter values from Section VII. During the simulation, the gust traversed along the boundary of the domain at a constant speed with the freestream flow to encounter the stationary airfoil. Since the gust profile was only specified on the domain boundaries, it was noticed that the gust deformed within the center of the domain. Figure 7(a) shows the vertical component of velocity at a probe location coincident with the leading edge of the airfoil for a simulation in which the airfoil was not present. Within the domain, the gust diffuses outward, increasing its gust width. Additionally, the CFD-simulated gust encounters the airfoil sooner than the intended ideal gust. An increase in the vertical velocity on the leading side of the gust and a reversal of the vertical velocity on the trailing side of the gust were observed. These features persisted with additional mesh refinement and were influenced by the height of the domain. More sophisticated techniques for gust simulation, such as the Field Velocity Method with gust source terms of [31], exist and are capable of providing profiles closer to the canonical shape of a sine-squared gust. Nevertheless, since the boundary-specified gust could be readily implemented in

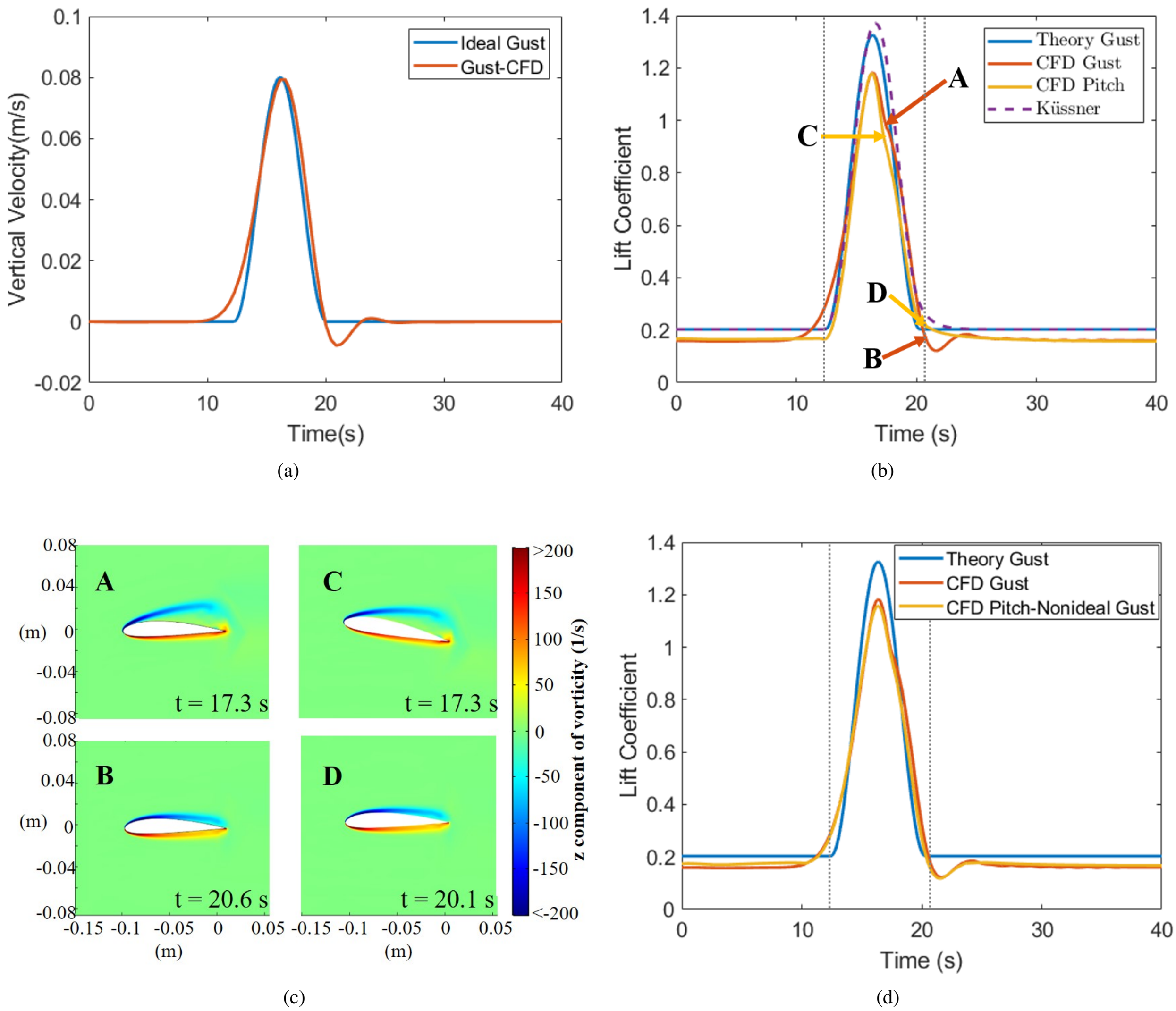

Fig. 7 CFD results: (a) gust profile simulated in CFD compared to the ideal gust shape specified at the boundary. (b) Lift curves from CFD simulations compared to predictions from effective angle of attack and Küssner's theory. (c) Surface plots of the out-of-plane component of vorticity at various points in time. (d) Lift curve for a simulation using a re-calculated pitching profile.

COMSOL Multiphysics® and the gust profile does not drastically differ from the canonical shape, this method of gust specification was used. Note that the CFD-simulated gust matches closely in amplitude with the desired gust shape.

Figure 7(b) compares the coefficient of lift histories for the gust encounter and the pitching airfoil, as well as the prediction from the proposed effective angle of attack theory in Section V. Figure 7(b) also contains the lift prediction of Küssner's theory [8] applied to the ideal gust shape. Küssner's theory has been shown to be a good predictor of the lift response for GR$\leq$ 0.5 [30]. The two curves calculated from CFD exhibit initial, final, and peak C_l values that are below the prediction from effective angle of attack. This discrepancy in the C_l magnitude may be attributed to the low Reynolds number, since simulations show that it diminishes as the flow speed is increased and potential flow theory agrees well with the lift values from CFD at the higher Reynolds number in Fig. 6. Notably, the lift coefficient curves for the gust encounter and the pitching maneuver match very close in peak amplitude and timing of the lift peak. The duration of the increase in lift was similar, differing by corresponding features in the vertical gust profile used for simulation in Fig. 7(a); the lift increase begins early and experiences a trailing dip later in the encounter. Both

CFD curves have slopes that are similar to the theoretical gust encounter prediction. However, unlike the theory-based curve, the CFD curves both exhibit a change in slope on the downward-sloping portion of the lift curve (see points A and C in Fig. 7(b)). Figure 7(c) displays the z-component of the vorticity field when the slope changes occur (see subplots A and C in Fig. 7(c)). The upper boundary layer rapidly separates from the airfoil as a shear layer of negative vorticity at this time. Later in the simulations, the shear layer re-attaches at points B and D in Fig. 7(b) for the gust and pitching maneuver, respectively. In Fig. 7(c), the flow structures created during separation and re-attachment are nearly identical for the gust-encountering airfoil and the pitching airfoil, which can be attributed to the close matching of effective angle of attack for these airfoils just prior to the moment of flow separation. However, this example represents a relatively benign case since the violation of the attached flow assumption occurs only once and in a limited manner; it is reasonable to expect a gust encounter with massive flow separation to yield a different flowfield behind the wing than a high-angle-of-attack maneuver would yield.

Although the simulated gust profile in Fig. 7(a) deviated from the ideal gust profile, it is possible to account for these deviations by re-calculating a pitching maneuver using the effective angle of attack matching in (65) for the non-ideal gust profile from CFD. Figure 7(d) shows the lift curve for a CFD simulation of the airfoil pitching according to the re-calculated maneuver. Very good agreement with the gust encounter profile was obtained.

IX. Conclusion

The paper presents a novel expression for a quasi-steady effective angle of attack from thin-airfoil theory that does not utilize the small-angle approximation or small-camber-slope approximation, although the small-camber assumption partially remains due to the projection of the bound vortex sheet onto the chord line. The expression includes kinematic effects related to pitching, plunging, and surging of the airfoil, as well as freestream nonuniformity. The expression is derived using the local angle of attack due to the relative flow and trigonometric identities so that these two approximations were not needed. Assumptions of attached flow and a thin airfoil still remain. The resulting expression properly encompasses existing expressions for effective angle of attack and also provides a new expression for the zero-lift angle for a cambered thin airfoil in steady-flow conditions. Predicted values of the zero-lift angle for cambered airfoils are compared to experimental data obtained from literature, showing good agreement. This paper also applies the proposed effective angle of attack expression to a problem of emulating a transverse gust encounter using a maneuvering airfoil with four different kinematic motions (i.e., pitching only, plunging only, and two different pitching and plunging combinations). The results of the proposed optimization framework provide an accurate solution for matching the effective angle of attack for an airfoil encountering a gust and another that maneuvers to mimic such an encounter, subject to the assumptions implicit in the effective angle of attack derivation. Computational Fluid Dynamics (CFD) simulations were performed. Steady-flow simulations validate the proposed theory and compare well with experimental data, with deviations attributable to modeling assumptions and viscous effects. Unsteady CFD simulations were performed to compare the lift response of an airfoil in a gust encounter to one of the four kinematic profiles that was derived to mimic a gust response. For the low gust ratio simulated and a small angle of attack pitching maneuver, the two lift responses show very good agreement due to the matching of the effective angle of attack. In ongoing work, we are extending the kinematic analysis of this paper to examine unsteady motion effects (i.e., acceleration effects), and we are pursuing experimental validation.

Acknowledgments

This work was partially supported by the National Science Foundation under grant CBET-2003999, monitored by program officer Dr. Ron Joslin. The authors gratefully acknowledge valuable discussions with Girguis Sedky, Matthew Ringuette, Jeff Eldredge, David Williams, Tarunraj Singh, James Chen, and Kunihiko Taira. The authors thank the anonymous reviewers for helping to improve this manuscript.

References

[1] Anderson, J. D., Fundamentals of Aerodynamics, 6th ed., McGraw-Hill Companies, 1984.

[2] von Kármán, T., "Airfoil Theory for Non-Uniform Motion," Journal of the Aeronautical Sciences, Vol. 5, No. 10, 1938, pp. 379–390. doi:10.2514/8.674.

[3] Theodorsen, T., "General Theory of Aerodynamic Instability and the Mechanism of Flutter," Tech. Rep. 496, National Advisory Committee for Aeronautics, 1935.

[4] Wagner, H., "Über die Entstehung des dynamischen Auftriebes von Tragflügeln," ZAMM-Journal of Applied Mathematics and Mechanics/Zeitschrift für Angewandte Mathematik und Mechanik, Vol. 5, No. 1, 1925, pp. 17–35.

[5] Sears, W. R., "Some Aspects of Non-Stationary Airfoil Theory and Its Practical Application," Journal of the Aeronautical Sciences, Vol. 8, No. 3, 1941, pp. 104–108. doi:10.2514/8.10655.

[6] Brunton, S. L., and Rowley, C. W., "Empirical State-Space Representations for Theodorsen's lift model," Journal of Fluids and Structures, Vol. 38, 2013, pp. 174–186.

[7] Brunton, S. L., Rowley, C. W., Taira, K., Colonius, T., Collins, J., and Williams, D. R., "Unsteady aerodynamic forces on small-scale wings: Experiments, simulations and models," 46th AIAA Aerospace Sciences Meeting and Exhibit, Paper 520, 2008. doi:10.2514/6.2008-520.

[8] Leishman, G. J., Principles of Helicopter Aerodynamics, Cambridge University Press, 2006.

[9] Sedky, G., Jones, A. R., and Lagor, F. D., "Lift Modeling and Regulation for a Finite Wing during Transverse Gust Encounters," AIAA SciTech Forum, Paper 1146, 2019. doi:10.2514/6.2019-1146.

[10] Peters, D. A., "Toward a Unified Lift Model for Use in Rotor Blade Stability Analyses," Journal of the American Helicopter Society, Vol. 34, No. 4, 1985, pp. 32–42.

[11] Peters, D. A., "Two-dimensional incompressible unsteady airfoil theory- an overview," Journal of fluids and structures, Vol. 24, 2008, pp. 295–312.

[12] Peters, D. A., Hsieh, M.-c. A., and Torrero, A., "A State-Space Airloads Theory for Flexible Airfoils," Journal of the American Helicopter Society, Vol. 52, No. 4, 2007, pp. 329–342.

[13] Brunton, S., Rowley, C., Taira, K., Colonius, T., Collins, J., and Williams, D., "Unsteady Aerodynamic Forces on Small-Scale Wings: Experiments, Simulations, and Models," 46th AIAA Aerospace Sciences Meeting and Exhibit, Paper 520, 2008.

[14] Ramesh, K., Gopalarathnam, A., Granlund, K., Ol, M. V., and Edwards, J. R., "Discrete-Vortex Method with Novel Shedding Criterion for Unsteady Aerofoil Flows with Intermittent Leading-Edge Vortex Shedding," Journal of Fluid Mechanics, Vol. 751, 2014, pp. 500–538. doi:10.1017/jfm.2014.297.

[15] Narsipur, S., Gopalarathnam, A., and Edwards, J. R., "Low-Order Model for Prediction of Trailing-Edge Separation in Unsteady Flow," AIAA Journal, Vol. 57, No. 1, 2019, pp. 191–207. doi:10.2514/1.J057132.

[16] Visbal, M. R., and Garmann, D. J., "Comparison of Pitch Versus Plunge Maneuvers of a Finite Wing," AIAA Aviation Forum, Paper 3334, Dallas, TX, 2019. doi:10.2514/6.2019-3334.

[17] Leung, J. M., Wong, J. G., Weymouth, G. D., and Rival, D. E., "Modeling Transverse Gusts Using Pitching, Plunging, and Surging Airfoil Motions," AIAA Journal, Vol. 56, No. 8, 2018, pp. 3271–3278. doi:10.2514/1.J056961.

[18] Biler, H., Badrya, C., and Jones, A. R., "Experimental and Computational Investigation of Transverse Gust Encounters," AIAA Journal, Vol. 57, No. 11, 2019, pp. 1–15. doi:10.2514/1.j057646.

[19] Sedky, G., Jones, A. R., and Lagor, F. D., "Lift Regulation During Transverse Gust Encounters Using a Modified Goman–Khrabrov Model," AIAA Journal, 2020, pp. 1–11. doi:10.2514/1.J059127, URL `https://arc.aiaa.org/doi/10.2514/1.J059127`.

[20] Naguib, A. M., and Koochesfahani, M. M., "Inviscid flow analysis of a circular cylinder traversing across an unbounded uniform-shear stream," Journal of Fluid Mechanics, Vol. 882, 2020, pp. A211–A2124. doi:10.1017/jfm.2019.820.

[21] Hammer, P. R., Visbal, M. R., Naguib, A. M., and Koochesfahani, M. M., "Lift on a steady 2-D symmetric airfoil in viscous uniform shear flow," Journal of Fluid Mechanics, Vol. 837, 2018, pp. R21–R211. doi:10.1017/jfm.2017.895.

[22] Kasdin, N., and Paley, D. A., Engineering Dynamics: A Comprehensive Introduction, 2nd ed., Princeton University Press, 2011.

[23] Stevens, B. L., Lewis, F. L., and Johnson, E. N., Aircraft Control and Simulation: Dynamics, Controls Design, and Autonomous Systems, John Wiley & Sons, 2015.

[24] Eldredge, J. D., Mathematical Modeling of Unsteady Inviscid Flow, Springer Nature Switzerland AG, Cham, Switzerland, 2019.

[25] Ramesh, K., Gopalarathnam, A., Edwards, J. R., Ol, M. V., and Granlund, K., "An Unsteady Airfoil Theory Applied to Pitching Motions Validated against Experiment and Computation," Theoretical and Computational Fluid Dynamics, Vol. 27, No. 6, 2013, pp. 843–864. doi:10.1007/s00162-012-0292-8.

[26] Katz, J., and Plotkin, A., Low-Speed Aerodynamics, 2nd ed., Cambridge University Press, Cambridge, 2001.

[27] Jacobs, E. N., and Sherman, A., "Airfoil Section Characteristics as Affected by Variations of the Reynolds Number," Tech. Rep. 586, National Advisory Committee for Aeronautics, 1939.

[28] Abbott, I. H., and von Doenhoff, A. E., Theory of Wing Sections: Including a Summary of Airfoil Data, Dover Publications, New York, NY, 1959.

[29] Jacobs, E. N., Ward, K. E., and Pinkerton, R. M., "The Characteristics of 78 Related Airfoil Sections from Tests in the Variable-Density Wind Tunnel," Tech. Rep. 460, National Advisory Committee for Aeronautics, 1933.

[30] Badrya, C., Baeder, J. D., and Jones, A. R., "Application of Prescribed Velocity Methods to a Large-Amplitude Flat-Plate Gust Encounter," AIAA Journal, Vol. 57, No. 8, 2019, pp. 3261–3273. doi:10.2514/1.J057978, URL https://doi.org/10.2514/1.J057978.

[31] Badrya, C., and Baeder, J., "Numerical Study of a Flat Plate Wing Response to Large Transverse Gusts at Low Reynolds Number," AIAA SciTech Forum, Paper 0638, 2019. doi:10.2514/6.2019-0638.

[32] Ogunbodede, O., Nandi, S., and Singh, T., "Periodic Control of Unmanned Aerial Vehicles based on Differential Flatness," Proceedings of the American Control Conference, 2018, pp. 2681–2686. doi:10.23919/ACC.2018.8430793.

[33] MATLAB version 9.6.0.1150989 (R2019a) Update 4, The Mathworks, Inc., Natick, Massachusetts, 2019.

[34] COMSOL Multiphysics reference manual, COMSOL Multiphysics®, v. 5.5. URL www.comsol.com.

[35] COMSOL Multiphysics®, "Particle Tracing in a Micromixer," , v. 5.5. URL https://www.comsol.com/model/download/654661/models.cfd.micromixer_particle_tracing.pdf.

[36] COMSOL Multiphysics®, "Flow Around an Inclined NACA 0012 Airfoil," , v. 5.5. URL https://www.comsol.com/model/download/636791/models.cfd.naca0012_airfoil.pdf.

[37] Ladson, C. L., "Effects of Independent Variation of Mach and Reynolds Numbers on the Low-Speed Aerodynamic Characteristics of the NACA 0012 Airfoil Section," Tech. Rep. 4074, NASA Langley Research Center, Hampton, VA, 1988.

[38] Grubb, A. L., Moushegian, A., Heathcote, D. J., and Smith, M. J., "Physics and Computational Modeling of Nonlinear Transverse Gust Encounters," AIAA Scitech 2020 Forum, 2020. doi:10.2514/6.2020-0080, URL https://arc.aiaa.org/doi/abs/10.2514/6.2020-0080.